THE STUDY OF ACOUSTIC PROPERTIES OF P_2O_5-DOPED SILICA FIBER

BY

PI-CHENG LAW

THESIS

Submitted in partial fulfillment of the requirements
for the degree of Master of Science in Electrical and Computer Engineering in the
Graduate College of the
University of Illinois at Urbana-Champaign, 2012

Urbana, Illinois

Adviser:

Research Professor Gary R. Swenson

ABSTRACT

Silica-based optical fibers have been applied to numerous fields. The interactions between acoustic phonons and the optical wave are involved in several of these applications. A significant stimulated scattering mechanism observed is stimulated Brillouin scattering (SBS), resulting in strong backward scattering typically within the optical fiber core. SBS has become one of the significant factors limiting the power transmitted in an optical fiber. Through investigating acoustic properties with temperature and strain effects, novel fibers can be developed by decreasing SBS of high power laser systems for optical remote sensing, or by increasing sensitivity to temperature or strain for distributed fiber-optic sensing systems.

This thesis presents measurements and modeling of the P_2O_5 doping effect on the acoustic damping and temperature sensitivity coefficients of silica fibers. The Brillouin gain spectrum of a highly P_2O_5-doped fiber is measured at different temperatures. Its thermo-acoustic coefficients (TAC) and thermo-optic coefficients (TOC) are determined. In addition, its acoustic velocity is found to be much less dependent on temperature. We present similar analysis for the P_2O_5 doping effect on the strain sensitivity coefficients of silica fibers. The strain-optic coefficient (SOC) and the strain-acoustic coefficient (SAC) of bulk P_2O_5 are determined by investigating the Brillouin gain spectrum of a heavily P_2O_5-doped fiber and a pure silica fiber at different strains. The Pockels coefficients p_{11} and p_{12} for bulk P_2O_5 are also estimated via Brillouin gain measurements.

The experimental data and analysis results are extremely useful for designing optical and acoustic profiles of optical fibers for any applications where Brillouin scattering occurs.

To my parents, Mr. Shih-Hung Lo and Mrs. Pi-Shiu Lo-Huang, and the Law (Lo) Family

who love and support me

ACKNOWLEDGMENTS

I would like to acknowledge Professor Gary R. Swenson and Dr. Peter D. Dragic for their full support. This work was supported in part by the Joint Technology Office (JTO) through their High Energy Laser Multidisciplinary Research Initiative (HEL-MRI) program entitled “Novel Large-Mode-Area (LMA) Fiber Technologies for High Power Fiber Laser Arrays” under ARO subcontract # F014252. Finally, I thank my research fellows and friends who have helped with my graduate life at the University of Illinois at Urbana-Champaign.

TABLE OF CONTENTS

LIST OF TABLES

LIST OF FIGURES

LIST OF ABBREVIATIONS

AD	Additive
AIP	Acoustic Index Profile
AOM	Acousto-optic Modulator
BFS	Brillouin Frequency Shift
BGC	Brillouin Gain Coefficient
BGS	Brillouin Gain Spectrum
ECDL	External-cavity Diode Laser
EDFA	Erbium Doped Fiber Amplifier
EPMA	Electron Probe Microanalysis
ESA	Electrical Spectrum Analyzer
FSR	Free Spectral Range
FWHM	Full Width at Half Maximum
FUT	Fiber under Test
HOAMs	Higher-order Acoustic Modes
LMA	Large Mode Area
LO	Local Oscillator
MCVD	Modified Chemical Vapor Deposition
MFD	Mode Field Diameter
RF	Radio Frequency
RIP	Relative Index Profile
RNF	Refracted Near Field
SAC	Strain-acoustic coefficient
SBS	Stimulated Brillouin Scattering
SOC	Strain-optic coefficient
SpBS	Spontaneous Brillouin Scattering
TAC	Thermo-acoustic coefficient
TOC	Thermo-optic coefficient

CHAPTER 1

INTRODUCTION

It is well known that silica-based optical fibers have been used for numerous applications. Several of these applications include interactions between acoustic phonons and the optical wave. An important stimulated scattering process that has been observed is stimulated Brillouin scattering (SBS), which leads to a highly-reflective distributed Bragg grating resulting from a propagating pressure wave, typically within the optical fiber core. More specifically, the light scattering occurs when the intensity of the light field affects the propagating medium where SBS effect is caused by the spatial and spectral overlap between the optical waves and the acoustic modes in the fiber waveguide. SBS effect has become one of the major limiting factors [1] on the amount of the power transmitted in an optical fiber due to increasing power required in the optical fiber core and relatively long interaction lengths for systems using narrow linewidth such as narrow linewidth fiber lasers used in optical remote sensing.

Recently innovative optical fibers with customized acoustic profiles have been designed specifically for some applications where Brillouin scattering may be encountered. The applications may require either its suppression or its utilization. SBS is useful in some cases. For example, distributed sensing uses either stimulated Brillouin scattering or spontaneous Brillouin scattering (SpBS) with Brillouin frequency shift (BFS) as a function of temperature [2,3,4]. In contrast, it is detrimental in some cases, such as in high power and narrow linewidth fiber lasers with a low SBS threshold [5,6]. Thus, many solutions are proposed including broadening the effective laser linewidth, designing optical fiber with an acoustic guiding layers [7], reducing effective fiber length by varying core size [8], dopant concentrations [9], temperature [10], or stress and strains [11], using large mode area fiber [12,13], designing dual cladding fiber [6] , etc.

Since SBS is strongly related to the acoustic properties, the acoustic profiles of the optical fiber can be manipulated for some SBS applications. In order to completely understand their

relationships, it is necessary to further study the acoustic properties of the optical fiber using Brillouin scattering method to precisely describe their connections and predict their behaviors under the different conditions.

For comprehending the relationship of the acoustic properties between dopants, a ternary-system fiber such as B_2O_3-doped germanosilicate fiber was investigated. Interestingly, an existing model was used to adequately explain viscosity effect on the anomalous Brillouin spectral widths observed in the experiments [14].

In order to realize how the anti-waveguide influences acoustic properties, a pure silica fiber with a pure silica core and F-doped cladding was studied. Since the acoustic velocity in the core is greater than that in the cladding, the fiber is acoustically antiguiding. It is found that the acoustic damping coefficient increases with increasing mode number and decreasing core diameter as well [15]. The waveguide loss also plays an important role on the acoustic attenuation affecting the observed spectral width.

Due to more common fibers as references in experiments, binary-system fibers such as Ge_2O_3-doped fibers are investigated. These optical fibers with different dopant concentrations and compositional profiles present different acoustic properties providing valuable temperature-dependent acoustic coefficients [16]. The coefficients can be used to design specialty fibers for desirable applications in temperature.

In addition, since the P_2O_5-doped fiber has not been studied yet in the literature, this thesis will completely study the thermo- and strain-acoustic properties of a P_2O_5-doped optical fiber through a series of experiments and analyses and determine the unknown thermo- and strain-acoustic coefficients. These acoustic coefficients will be utilized to design fibers for the sensing applications in temperature and strain.

Investigating the different doped silica fiber is a pathway to build the foundation of the generalized model. The generalized model will include the relation of optical and acoustic parameters vs. temperature or strain. It provides fiber designers with a predictable direction to manipulate the compositional profile and further create the desirable properties for any applications in temperature and strain. In addition, novel optical fibers with tailored acoustic profiles can also be designed specifically for applications associated with Brillouin scattering suppression. Therefore, it is essential and obligatory to understand these different fibers for developing a potential generalized model in the future.

1.1 Motivation of Thermo-Acoustic Experiments

Necessary in the process of designing an acoustic profile is the knowledge of how potential dopants influence the relevant thermo-acoustic parameters in a host material, such as silica. Much less has been done to characterize Brillouin spectral width related to attenuation coefficient and how the thermo-acoustic coefficient (TAC) and thermo-optic coefficient (TOC) are influenced by these dopants [17], while publications can be found to show how some common dopants influence the acoustic velocity in SiO_2 [18]. This data is particularly significant, for example, when the large acoustic damping coefficients associated with some dopants can be used as a degree-of-freedom in the design of a specialty fiber. Moreover, clearly understanding the TACs and TOCs of the various dopants can lead to the development of novel optical fibers for distributed temperature sensor applications.

An analysis was done with the measurement of the Brillouin gain spectrum (BGS) of a heavily GeO_2-doped optical fiber [19]. From the measured BGS, and a fit to a simple materials model for GeO_2-doped fibers, it was able to extract an acoustic attenuation coefficient for bulk GeO_2 [20]. This value was modified due to a more accurate compositional profile [21]. This acoustic attenuation value increases with acoustic-frequency-squared for GeO_2-doped fibers [22]. In addition to other basic material parameters for the bulk material, this data point can then be used to calculate and design sets of relevant acoustic profiles for arbitrary compositional profiles, and can be extended to include systems of multiple dopants.

A similar analysis of a P_2O_5-doped optical fiber is presented in this thesis. It is found that, for the purposes of modeling P_2O_5-doped fibers, including P_2O_5-doped inner cladding layers, bulk phosphorus oxide has an acoustic attenuation coefficient (α_p) similar to, but larger than, that of bulk GeO_2. Both of these values are larger than that of silica [21]. Meanwhile, the spectral width of the L_{01} acoustic mode of a P_2O_5-doped optical fiber is also found to decrease with temperature increase at a rate similar to that of GeO_2-doped optical fiber.

In addition, the experimental results indicate that, for the L_{01} acoustic mode, the Stokes shift increases with temperature increase. Using similar measurements on each of the four observed acoustic modes located in the core, it is found that the TAC of the bulk acoustic velocity of P_2O_5

is less than that of silica. In order to obtain this coefficient from the P_2O_5 and SiO_2 co-doped oxide glass, a pure SiO_2-core (Sumitomo Z Fiber) is measured to obtain the temperature-dependence of the pure silica component. The SiO_2-P_2O_5 system is modeled in an additive way to determine the P_2O_5 value. The TAC value for silica is in good agreement with previous results on the bulk material [23,24], providing a large degree of confidence in the P_2O_5 value.

These temperature-dependent coefficients are very useful for designing specialty fibers of sensor applications in temperature. For instance, utilizing the determined temperature-dependent coefficients, a composition is found whose Stokes shift dependence on temperature is minimized [25]. This design reveals that this fiber is only sensitive to a specific physical measureable quantity (e.g. strain) for a specific sensing application (e.g. transport monitoring).

1.2 Motivation of Strain-Acoustic Experiments

From the measured BGS of a P_2O_5-doped optical fiber and a fit to a simple materials model for P_2O_5-doped fibers [20], we can extract an acoustic velocity, acoustic attenuation, and thermo-acoustic coefficient for bulk P_2O_5. These values for the bulk material can be used to calculate and design sets of relevant acoustic profiles for arbitrary compositional profiles for distributed temperature sensing applications.

Similarly, there are many examples using Brillouin frequency shift as a function of strain for the distributed pressure sensing uses [26]. Therefore, a similar analysis is presented for the tensile strain effect on a P_2O_5-doped optical fiber to derive a strain-optic coefficient (SOC) and strain-acoustic coefficient (SAC) for bulk P_2O_5 and pure silica. These values are particularly important because, when associated with dopants and concentrations, they can be used as a degree-of-freedom in the design for a strain-sensitive fiber. Furthermore, comprehending these coefficients of the various dopants can lead to the development of novel optical fibers for distributed strain sensor applications.

The SOC values of bulk SiO_2 and silica fiber have been reported in [27]. However, an extensive search finds that the SOC of bulk P_2O_5 (calculated from the Pockels coefficients, $p_{11}$and p_{12}, and the Poisson ratio, σ, via $p_{12}-\sigma\cdot(p_{11}+p_{12})$) is not reported in the literature even

though the strain effect on acoustic frequency and spectral widths has been studied for bulk materials and silica fibers [28,29,30].

Like the previous work for TAC, we need this SOC of bulk P_2O_5 to determine its SAC. In order to obtain the SAC from P_2O_5 and SiO_2 co-doped oxide glass, a pure SiO_2-core (Sumitomo Z Fiber) and a P_2O_5-doped silica fiber were first tested to obtain the strain-dependency of the SiO_2 and P_2O_5. Therefore, the SOC of P_2O_5-doped silica fiber and pure silica fiber (Z Fiber) are measured utilizing the strain-dependent free spectral range (FSR) of a fiber ring laser [31,32]. The SOC value for pure silica fiber is in good agreement with previous measurements on the optical fiber [27], providing a large degree of confidence for our formalism in the P_2O_5 value. The SiO_2-P_2O_5 system is modeled using an additive model [20] to fit the SOC values of P_2O_5-doped silica fiber, and thus it is able to extract the SOC of bulk P_2O_5. This SOC of P_2O_5-doped silica fiber is slightly lower than the pure silica value, but both are much higher than the SOC of bulk P_2O_5. In addition, through Brillouin gain measurements one can obtain the measured Pockels coefficient (p_{12}) of P_2O_5-doped fiber and estimate thus the measured Pockels coefficients for bulk P_2O_5. This p_{12} could further help extract p_{11} from the SOC of bulk P_2O_5 using a well-known Poisson ratio of bulk P_2O_5 [33] in an additive way with considerable error. However, this thesis is the first attempt to determine these values for bulk P_2O_5 and of P_2O_5-doped fiber.

Experimental results on the Stokes frequency shift with strain changes for P_2O_5-doped silica fiber and SMF-28 indicate that, for the L_{01} acoustic mode, the Stokes shift increases approximately linearly with elongation. While the rate of standard GeO_2-doped SMF-28 fiber is higher, both of these values are less than that of pure silica fiber (Z Fiber). The rate is found to be much less dependent on strain in P_2O_5 than in SMF-28 and in pure silica fiber as well. Utilizing these SOC coefficients and measurements of the BGS at various strains on each of the four observed acoustic modes located in the core, in the same additive way the modeled and unique slopes of the Stokes-shift-versus-strain curves fit the measured values of the four observed acoustic modes. By the relation of acoustic velocity versus strain, one can determine the SAC of bulk P_2O_5, which is found to be much lower than that of bulk SiO_2.

The SOC and SAC coefficients will help to design novel optical fibers for distributed strain sensor applications. For instance, utilizing the determined coefficients, a composition is found and its Stokes shift dependence on strain is suppressed. This composition provides the specialty

fiber with high sensitivity to a specific physical measureable quantity for a specific sensing application.

1.3 Thesis Outline

This thesis mainly focuses on the acoustic properties of the P_2O_5-doped optical fiber. Chapter 1 addresses the background of SBS and the motivations of thermo-acoustic properties and strain-acoustic properties which are driven by any kind of the sensing applications. Chapter 2 introduces SBS theory and how SBS is related to the acoustic properties of optical fibers as well as how material characteristics of the dopant and geometric properties of the waveguide affect the acoustic properties of optical fibers. In addition, temperature and pressure effect are presented via the thermo- and strain-acoustic coefficients of optical fibers. Finally, an additive model introduced here has been widely applied for optical index, acoustic velocity, mole density, and photoelastic coefficient in the analyses of composite optical fibers. Chapter 3 will present the temperature effect on the P_2O_5-doped optical fiber from experimental setups and fiber sample information, as well as measurements and analyses of Brillouin gain spectra at room and other temperatures. Additionally, the acoustic attenuation, thermo-optic and thermo-acoustic coefficients are studied and determined. Chapter 4 will exhibit the strain effect on the P_2O_5-doped optical fiber through experimental setups, as well as measurements and analyses of Brillouin gain spectrum at room and other temperatures. Specifically, the strain-optic and strain-acoustic coefficients never reported before are completely studied and obtained. Chapter 5 will summarize the research achievements and elucidate the future research directions for study of the acoustic properties for optical fiber.

CHAPTER 2

THEORY AND MODEL

2.1 Brillouin Scattering

Many applications of silica-based optical fibers are related to interactions between phonons and photons. A key stimulated scattering is stimulated Brillouin scattering. Thermal noise phonons in the medium give rise to random acoustic pressure waves within the fiber core. The light wave interacts with acoustic waves to enhance a highly-reflective distributed Bragg grating via electrostriction effect, and it manifests a propagating acoustic wave in the medium. The light scattering occurs and increases in intensity when the light field interacts with the acoustic pressure wave via a specific Bragg condition [34]. SBS can be observed when the light scattering intensity is higher than a threshold value. Figure 2.1 illustrates Brillouin scattering mechanisms including incident light, scattering light, and acoustic wave. This image is taken from [35].

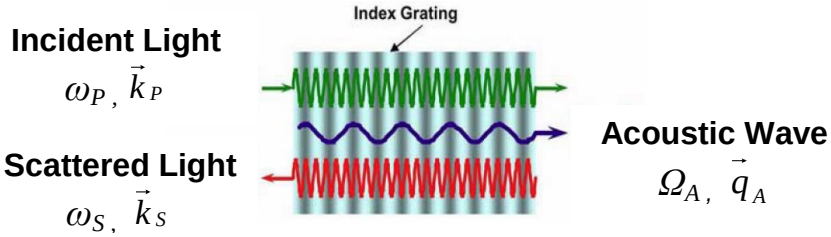

Figure 2.1: Brillouin scattering in an optical fiber results from Bragg scattering of an induced acoustic wave.

Both the energy and momentum must be conserved during Brillouin scattering. The frequencies and wave vectors of three waves are related by $\Omega_A=\omega_P-\omega_S$ and $\vec{q}_A=\vec{k}_P-\vec{k}_S$. Ω_A and $\vec{q}_A$ are Stokes frequency shift (acoustic frequency, v_B) and wave vector of acoustic phonons. ω_P and $\vec{k}_P$ are the pump frequency and wave vector of the seed laser. ω_S and $\vec{k}_S$ are Stokes frequency and wave vector of scattered light. They satisfy the dispersion relation, $q_A=2k_P\sin(\theta/2)$,

assuming $k_P \cong k_S$. θ is the angle between the incident and the scattered light. The maximum Brillouin scattering is backward scattering (θ=180°) and there is no forward scattering (θ=0°) in optical fibers which guide backward and forward scattering, so $\Omega_A = q_A V_A = 2V_A k_P$ and $\nu_B = \Omega_A/2\pi = 2n_o V_A/\lambda_o = V_A/\lambda_A$. V_A is the acoustic velocity, n_o is the refractive index of the scattering media, λ_o is the wavelength of the incident light in air, and λ_A is the acoustic wavelength. The acoustic wave associated with ν_B causes a periodic modulation of the refractive index scattering with the pump wave matching the Bragg condition, $\lambda_A = \lambda_o/2n_o$.

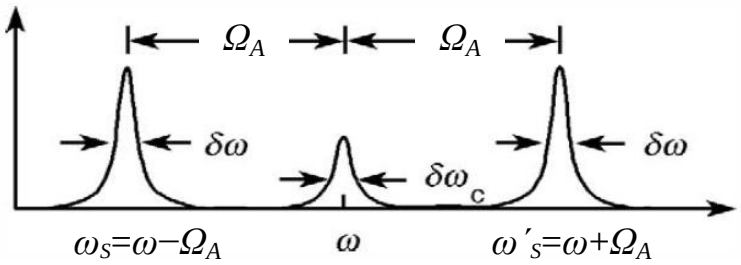

Figure 2.2: Spectrum of Stokes (ω_S) and anti-Stokes (ω'_S) Brillouin scattering and Rayleigh scattering (ω).

Figure 2.2 shows a Brilluoun gain spectrum. This image is taken from [34]. The scattered light down-shifts by Ω_A to ω_S as Stokes scattering due to the Doppler shift associated with a grating moving at V_A. In contrast, the scattered light up-shifts by Ω_A to ω'_S as anti-Stokes scattering due to the Doppler shift associated with a grating moving at $-V_A$. Additionally, the BGS has the Lorentzian spectral profile given by

$$\sum_m g_B(\nu_{B,m}) \frac{(\Delta\nu_{B,m}/2)}{(\nu - \nu_{B,m})^2 + (\Delta\nu_{B,m}/2)^2} \Gamma_m \qquad (2.1)$$

if there are m acoustic modes. The spectral profile with Brillouin spectral width (FWHM) $\Delta\nu_B$ ($=\delta\omega/2\pi$) is caused by the acoustic wave decay as $\exp(-t/\tau_p)$ where τ_p is lifetime of the acoustic wave or phonon. $\Delta\nu_B$ relates to τ_p by $\Delta\nu_B = 1/(\pi\tau_p)$. $g_B(\nu_B)$ is the Brillouin gain coefficient (BGC) given by

$$g_B(\nu_B) = 2 \cdot \pi \cdot n_o^7 \cdot p_{12}^2 / c \cdot \lambda_o^2 \cdot \rho \cdot V_A \cdot \Delta\nu_B \qquad (2.2)$$

where p_{12} is the photoelastic coefficient, ρ is the mass density, and c is the light speed. Γ_m is the square of the normalized scattering integral between the optical and acoustic fields for acoustic mode m. Due to the viscosity of the materials, the acoustic wave function propagating in the z direction includes the material damping coefficient (α_m) term as $\exp(-\alpha_m z)$ in addition to the wave vector term, $\exp(-iq_A z)$. The amplitude of the acoustic wave decays to $\exp(-1)$ by a traveling distance $1/\alpha_m$. The decay time of the acoustic wave is the traveling distance divided by acoustic velocity and represents the lifetime τ_p of this acoustic wave ($1/\alpha_m/V_A=\tau_p$). Therefore, given $\Delta\nu_B=1/(\pi\tau_p)$ mentioned earlier, $\Delta\nu_B=\alpha_m V_A/\pi$. In addition, when waveguide loss γ_{wg} is comparable to α_m for acoustic antiguide fibers, we should consider not only α_m but also γ_{wg} effect on $\Delta\nu_B$ because the amplitude of acoustic wave also decays with $\exp(-\gamma_{wg} z)$ and thus γ_{wg} decreases the acoustic-optic interaction time. That is, the BGS is a convolution of two Lorentzian functions related to each of α_m and γ_{wg}. Both are exponential losses, so α_m can be lumped with γ_{wg}. Therefore, the Brillouin spectral width is related to acoustic velocity (V_A), material damping coefficient (α_m), and waveguide loss (γ_{wg}) by $\Delta\nu_B = V_A(\alpha_m+\gamma_{wg})/\pi$.

New optical fibers with tailored acoustic profiles have been studied for some applications where Brillouin scattering may occur. The applications may require either its suppression or its utilization. For utilization cases, temperature sensing uses Brillouin frequency shift as a function of temperature [3,4] and strain sensing uses BFS as a function of strain due to high sensitivity to the tensile strain [36].

For suppression cases, such as high power and narrow linewidth fiber lasers [5,6], in the fiber waveguide the optical waves and the acoustic modes overlap in the space and spectrum to cause SBS. The SBS has become one of the major limiting factors on the power transmitted in an optical fiber due to increasing power demand in the optical fiber core and relatively long interaction lengths required for optical remote sensing systems operating at narrow linewidth.

The SBS threshold power P_{th} given by $P_{th}=21A_{eff}/[L_{eff}\, g_B(\nu_{B,max})\, \Gamma_m]$ [1,37] can be introduced to find the possible solutions. $A_{eff}=2\pi(\int^{\infty}_0|E(r)|^2 r dr)^2/\int^{\infty}_0|E(r)|^4 r dr$, where $E(r)$ is the electric field of the optical mode. $L_{eff}=[1-\exp(-\alpha_o L)]/\alpha_o$ where $L_{eff}=1/\alpha_o$ if $\alpha_o L>>1$, $L_{eff}=L$ if $\alpha_o L<<1$, α_o is the optical fiber loss, and L is the fiber length. To suppress the SBS we can manipulate the effective area A_{eff}, the effective length L_{eff}, the Brillouin gain coefficient $g_B(\nu_{B,\,max})$, and the overlap integral Γ_m to increase the SBS threshold power and thus suppress SBS.

Therefore, many solutions including broadening the effective laser linewidth are proposed to decrease g_B scaled by $\Delta\nu_B/(\Delta\nu_B+\Delta\nu_L)$ when the laser linewidth ($\Delta\nu_L$) is greater than the Brillouin line width ($\Delta\nu_B$) [38], designing the optical fiber with an acoustic guiding layer to reduce the overlap integral [7], reducing the effective fiber length by varying core sizes [8], dopant concentrations [9], temperatures [10], or stresses and strains [11], using the large mode area fiber [12,13], or designing the dual cladding fiber [6], etc.

Since SBS is strongly related to the acoustic properties, the acoustic profiles of the optical fiber can be manipulated for some SBS applications. In order to completely comprehend the relationships between dopants and the acoustic profiles, it is necessary to further study the acoustic properties, ν_B, V_A, $\Delta\nu_B$, α_m, etc., in the optical fibers comprising different dopants using the Brillouin scattering method. Furthermore, understanding these different fibers is important because it can develop a generalized model to precisely describe how dopants affect these properties and predict their behaviors under the different conditions. Therefore, a ternary-system fiber, Boron doped germanosilicate fiber, was studied owing to its complexity of the multiple dopants [14]. An antiguding fiber, pure silica fiber, was investigated to realize how the anti-waveguide influences acoustic properties [15]. We have also investigated binary-system fibers because GeO_2-doped silica fibers are more common [16].

In this thesis, the thermo- and strain-optic coefficients of P_2O_5-doped silica fiber will be discussed. Since this fiber has not been studied yet in the literature, it is useful to investigate the acoustic properties of P_2O_5-doped silica fiber.

2.2 Waveguide and Dopant Effects

It is well known that optical fibers act as acoustic waveguides. Optical and acoustic waveguide and dopant effects on the fiber are not mutually exclusive; thus, the waveguide and dopant need to be considered simultaneously. The waveguide theory and dopant model relate the optical fiber to acoustic waveguide effects [39].

The waveguiding properties are largely set by the dopants in the system. Optical fibers can be acoustic waveguides or antiguides. Their acoustic profiles, like the optical index profiles, can

be graded or step-like. Acoustic cores can have profiles that consist of multiple layers or are multiply-cladded, much like optical waveguides.

Similarly to an optical fiber, the properties of an acoustic waveguide can be calculated from an eigenvalue problem utilizing the various boundary conditions of the system. Thus, if an acoustic profile is known, its acoustic waveguiding properties can be predicted. On the contrary, if a known acoustic property is desired, one can work through the theory to determine an acoustic profile to achieve the desired result.

All of the acoustic modes contribute to an overall Brillouin gain profile, so all significant acoustic modes of a tailored structure should be analyzed. Along these lines, we can tailor an acoustic profile to manipulate acoustic modes and preserve optical modes, and thus influence the Brillouin gain profile.

In order to assist in realizing the acoustic properties of the optical fiber, the Brillouin gain spectrum is investigated. The BGS includes two important parameters in addition to the Lorentzian function. One is the BGC, $g_B(\nu_m)$, inversely proportional to a material damping coefficient (α_m) and a waveguide loss coefficient (γ_{wg}) where ($\alpha_m+\gamma_{wg}$) is proportional to the Brillouin spectral width ($\Delta\nu_B$). Therefore, the BGC decreases with increasing γ_{wg} due to the two being inversely dependent. For an acoustic waveguiding fiber, γ_{wg} can be neglected since it is usually much smaller than α_m. In contrast, the acoustic antiguide nature of the fiber, $\gamma_{wg,}$ should be considered since it can be comparable to α_m. The other key parameter is the volume scattering integral, which is the overlap integral of the acoustic mode with the optical mode. It affects the BGS via a Γ_m which is the square of the normalized scattering integral and is unique for each acoustic mode *m*.

Different dopants with different optical and acoustic properties can be used to change the acoustic profile and thus manipulate the overlap integral value. Through the SBS threshold P_{th} equation described previously, we can estimate the SBS effect and then tailor the acoustic properties, i.e. an acoustic index profile (AIP) of an optical fiber, to maximize or minimize $g_B(\nu_m)$ and Γ_m of certain strength for a specific system or application.

Clearly imperative in the process of designing an acoustic profile is the knowledge of how potential dopants influence the relevant acoustic parameters in a host material, such as silica (SiO_2). Many publications can be found. They show that how some common dopants influence the acoustic velocity [18], optical index [40], and acoustic index [7].

Table 2.1: Dopant's effects on the optical refractive index, acoustic velocity, and acoustic refractive index.

		GeO_2	P_2O_5	TiO_2	B_2O_3	F_2	Al_2O_3	Y_2O_3	Yb_2O_3	Er_2O_3
Optical index	n_o	↑	↑	↑	↓	↓	↑	↑	↑	↑
Acoustic velocity	V_A	↓	↓	↓	↓	↓	↑	↑	↓	↓
Acoustic index	n_A	↑	↑	↑	↑	↑	↓	↓	↑	↑

Table 2.1 shows the effect of some common dopants and their effect on the optical and acoustic indexes. The upward pointing arrow means that the parameter value of the dopant is higher than that of pure silica and the downward pointing arrow means that the parameter value of the dopant is lower than that of pure silica. In order to draw the analogy with optical fields, an effective acoustic refractive index has to be introduced. Obviously, this implies that an increased acoustic index value represents a decreased acoustic velocity. Thus, to achieve an acoustic guiding layer, dopants such as GeO_2, P_2O_5, B_2O_3, or F_2 are used in the acoustic layer (such as the core). In contrast, Al_2O_3 is used to be an acoustic anti-guiding layer.

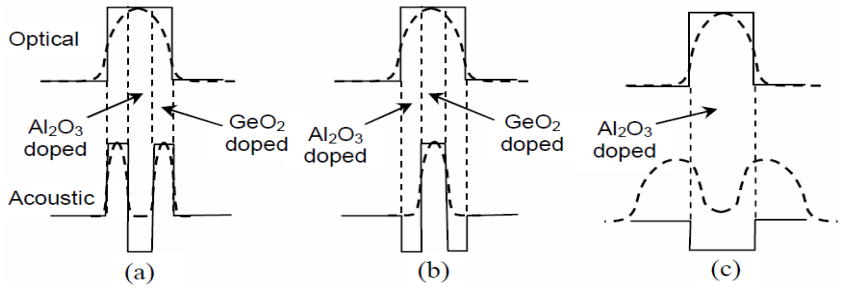

Figure 2.3: Al_2O_3 and GeO_2 dopants can reduce the overlap between optical refractive index and acoustic refractive index.

Figure 2.3 shows how Al_2O_3 and GeO_2 co-dopants can be used to reduce the overlap between optical mode and acoustic mode. This image is taken from [13]. In Figure 2.3(a) the inner core is doped with more Al_2O_3 while the outer core is doped with more GeO_2, so the optical mode resides in the whole core, but the acoustic mode is only confined in the outer core. Thus, the overlap integral is reduced. In Figure 2.3(b) the inner core is doped with GeO_2 while the outer core is doped with Al_2O_3, although Al_2O_3 and GeO_2 co-dopants co-exist. The optical mode resides in the whole core, but the acoustic mode is only confined in inner core. As a result,

the overlap integral is reduced significantly. In Fig 2.3(c) we can choose Al_2O_3 in the core to increase the optical index but decrease the acoustic index. Likewise, we can choose F_2 in the cladding to decrease the optical index but increase the acoustic index. Both choices cause the acoustic mode to be antiguided in the core, so the interaction between the optical mode and the acoustic mode is reduced.

In addition, other dopants, Yb_2O_3 and Er_2O_3, behave like GeO_2 [41] and Y_2O_3 behaves like Al_2O_3 [42]. However, the relative concentrations of these dopants must be carefully chosen to achieve the desired acoustic and optical index profile. Although the effect of several dopants on the acoustic velocities was reported [18], the exact change in these values as a function of doping concentration is a sensitive function of the exact fiber manufacturing process. Therefore, experimental characterization is necessary for each manufacturing procedure of the fiber.

However, much less work has been done to characterize how the dynamic viscosity, affecting the Brillouin spectral width, is influenced by these dopants [17]. This data is particularly important when the large acoustic damping coefficients associated with some dopants can be used as a degree-of-freedom in the design of a specialty fiber.

Therefore, this thesis will characterize the acoustic damping coefficients of P_2O_5-doped silica fiber via measurable acoustic quantities. Meanwhile, we study the thermo- and strain-optic coefficients of P_2O_5-doped silica fiber since this fiber has not been studied yet in the literature. The temperature and strain effects will be discussed in section 2.3. Additionally, a simple model has been developed to predict these various properties including the refractive index, acoustic velocity, molar mass, mass density, and material damping coefficient, and to calculate the BGC [43]. Interestingly, it can provide generally accurate prediction of the BGC of GeO_2-doped silica fibers. This model will be introduced in section 2.4 and applied to the analysis of the thesis.

2.3 Temperature and Strain Effects

In addition to these parameters, mentioned in section 2.1 and 2.2, mainly related to the dopant concentration profile, it is worth considering the temperature and strain as variables of the acoustic parameters. The temperature and strain effect on the acoustic properties of optical fibers can be engineered for the design of a specialty fiber in specific applications. Therefore, in order

to comprehend their relationships, through experiments and simulations, a pure silica fiber [15], GeO_2-doped silica fibers [16], and B_2O_3-doped silica fibers were investigated [14]. This thesis will focus on the thermo-acoustic and strain-acoustic properties of a P_2O_5-doped silica fiber.

The temperature-dependent acoustic frequency and spectral width are measured to link some of the acoustic parameters (acoustic velocity, acoustic attenuation, acoustic or optical index, etc.) to temperature. Gaining these temperature-dependent parameters is extremely useful to design a temperature sensor or a distributed temperature sensing system.

It is well known that $\nu_B=2n_oV_A/\lambda_o$ where ν_B is the acoustic frequency (Stokes frequency shift), V_A is the acoustic velocity, n_o is the refractive index of the scattering media, λ_o is the wavelength of the incident light in air. Assuming that λ_o is independent of temperature, the temperature dependence of acoustic frequency, taking the derivative with respect to T, is given by [2]

$$\frac{d\nu_B(T)}{dT}=\frac{2}{\lambda_o}\left[V_A(T)\frac{dn_o(T)}{dT}+n_o(T)\frac{dV_A(T)}{dT}\right]. \tag{2.3}$$

Here, dn_o/dT is defined as thermo-optic coefficient (TOC= dn_o/dT) and dV_A/dT is defined as thermo-acoustic coefficient (TAC= dV_A/dT). Therefore, assuming that the acoustic frequency is a linear function of temperature, the acoustic frequency can be written as

$$\nu_B(T)=\nu_B(T_o)+\frac{d\nu_B(T)}{dT} \tag{2.4}$$

where $\nu_B(T_o)$ is the acoustic frequency at temperature T_o and T_o is a reference temperature such as room temperature, and $d\nu_B/dT$ is the temperature dependence of acoustic frequency.

The temperature-dependent Stokes frequency shift as a measurable quantity can be utilized to detect the temperature variation. In addition, since both terms will influence the Stokes frequency shift changing with temperature, TOC and TAC will be a degree of freedom to manipulate the characteristics of $d\nu_B/dT$ and thus design a specialty fiber for specific applications. Furthermore, Equation (2.4) shows that a large or small $d\nu_B/dT$ value means some dopant in the silica fiber makes the optical fiber highly sensitive or insensitive to temperature variation. Meanwhile, concentration of the dopant will positively or negatively influence the

thermal sensitivity of the silica fiber. Therefore, $d\nu_B/dT$ is a function of dopants and their concentrations. The composite relations could provide more degrees of freedom to customize a desirable fiber. Thus, it is necessary to investigate their complex connections.

In addition to simply using Brillouin frequency shift to sense the temperature variation [2,3], the other way is using two acoustic modes, core mode and cladding mode [4], which differently respond to temperature change due to the different dopants or different dopant concentrations. Meanwhile, it is measureable that the beat frequency in the order of radio frequency (RF) varies adequately with temperature. Through tailoring the acoustic and optical interactions, gain equalization can be achieved as well. Thus, one can utilize the different responses (beat frequency) to temperature to design a temperature sensor or a distributed temperature sensing system. Alternatively, the differential RF power measurements of the beat signal such as a two- or three-frequency approach may be appropriate to monitor temperatures [44]. Extending the similar concept, one can utilize multiple acoustic modes in multiple layers or multiple Stokes frequencies in the fiber which differently shift with temperature variation [39]. Due to multiple acoustic modes to sense the temperature variation simultaneously, the approach could increase the accuracy of measurements and decrease the uncertainty of temperature variation or add a new dimension to multiple-channel systems.

In Equation (2.3) the temperature dependence of acoustic frequency is related to TOC and TAC. By tailoring the acoustic profile, TOC and TAC can be manipulated to change the temperature sensitivity of the acoustic frequency. One can harness the concentration variation of dopants and waveguide (core and cladding layers) design of optical fiber to gain the desirable acoustic profile. Therefore, it is important to determine the TOC and TAC of a bulk dopant for design of an appropriate acoustic profile in an additive way with other dopants. In Chapter 3, TOC of bulk P_2O_5 will be introduced and thus TAC can be determined via TOC. The TAC provides an important degree of freedom to design the compositional profile of optical fiber with a high sensitivity to temperature for temperature sensing applications.

Similarly, the strain effect on optical silica fiber as strain sensors is widely applied to monitor the transport systems and constructions such as rails, bridges, tunnels, and buildings [26,39]. Mainly utilizing strain to shift the acoustic frequency away from its strain-free frequency, one can monitor the strained event and locate the strained position to maintain the transport systems.

The strain dependence of acoustic frequency is written as [26]

$$\nu_B(\varepsilon) = \nu_B(\varepsilon = 0) + \frac{d\nu_B(\varepsilon)}{d\varepsilon} \cdot \varepsilon \tag{2.5}$$

where $\nu_B(\varepsilon)$ is the acoustic frequency under strain ε, $\nu_B(\varepsilon = 0)$ is the acoustic frequency with free strain ε (=0), $d\nu_B(\varepsilon)/d\varepsilon$ is the strain sensitivity of acoustic frequency, and ε is the strain.

Assuming that λ_o is independent of temperature, after $\lambda_o \nu_B/2 = n_o V_A$ takes the derivative with respect to strain ε, the strain sensitivity of acoustic frequency is given by

$$\frac{\lambda_o}{2}\frac{d\nu_B(\varepsilon)}{d\varepsilon} = V_A(\varepsilon)\frac{dn_o(\varepsilon)}{d\varepsilon} + n_o(\varepsilon)\frac{dV_A(\varepsilon)}{d\varepsilon}. \tag{2.6}$$

Here, $dn_o/d\varepsilon$ is defined as strain-optic coefficient (SOC= $dn_o(\varepsilon)/d\varepsilon$) and $dV_A(\varepsilon)/d\varepsilon$ is defined as strain-acoustic coefficient (SAC= $dV_A(\varepsilon)/d\varepsilon$). Both SOC and SAC govern the characteristics of the strain-dependent acoustic frequency. They give more degrees of freedom to design an adequate $d\nu_B(\varepsilon)/d\varepsilon$ in desirable applications. Moreover, Equation (2.5) indicated that a large or small $d\nu_B(\varepsilon)/d\varepsilon$ value means some dopant in the silica fiber makes the optical fiber highly sensitive or insensitive to strain variation. Meanwhile, concentration of the dopant will positively or negatively influence the strain sensitivity of the silica fiber. Therefore, $d\nu_B(\varepsilon)/d\varepsilon$ is a function of dopants and their concentrations. The composite relations could provide more degrees of freedom to tailor a desirable fiber for specific applications. Thus, it is useful to investigate their complex connections.

In Equation (2.6) the stain dependence of acoustic frequency is simply related to SOC and SAC. Through tailoring the acoustic profile, SOC and SAC can be manipulated to change the strain sensitivity of acoustic frequency. One can use concentration variation of dopants and waveguide (core and cladding layers) design of optical fiber to obtain the desirable acoustic profile. Therefore, it is important to determine the SOC and SAC of a bulk dopant for design of an appropriate acoustic profile in an additive way with other dopants.

In addition, SOC is determined by Pockels coefficients and Poisson ratio [45] and for optical fiber [46] is defined by

$$\frac{dn_o(\varepsilon)}{d\varepsilon} = \frac{1}{2} n_0^3 \left[(p_{11} + p_{12}) \cdot \sigma - p_{12} \right] \qquad (2.7)$$

which is calculated from the Pockels coefficients, p_{11} and p_{12}, the Poisson ratio, σ, and the zero-strain refractive index, n_o. It is noted that in Chapter 4 SOC only represents $p_{12} - (p_{11} + p_{12}) \cdot \sigma$ for convenience to determine the Pockels coefficients. Additionally, the other Pockels coefficients $p_{44} = (p_{11} - p_{12})/2$ [47].

After obtaining the Pockels coefficients of dopant, the SOC can be determined and it easily estimates the SOC of the doped silica fiber in an additive way. However, despite an extensive literature search, a reported SOC of bulk P_2O_5 could not be found while SiO_2, B_2O_3, and GeO_2 are reported in the literature. A determination of SOC and an estimation of p_{11} and p_{12} will be discussed in Chapter 4. It has to be pointed out that the significant digits of Pockels coefficients and Poisson ratio could influence $dn_o(\varepsilon)/d\varepsilon$ and dominate $dv_B(\varepsilon)/d\varepsilon$ via the multiplication of acoustic velocity $V_A(\varepsilon)$ since this acoustic velocity is typically more than a few thousands of m/s. Therefore, the uncertainty should be considered in estimates of the Pockels coefficients and Poisson ratio. On the other hand, the significant digits of the refractive index are also important because $dV_A(\varepsilon)/d\varepsilon$ has a large value.

In Chapter 4, the SOC of bulk P_2O_5 will be introduced and determined through measurements and simulation of P_2O_5-doped silica fiber and pure silica fiber. Given the SOC of bulk P_2O_5, the SAC can be determined. The SOC and SAC provide important degrees of freedom to design the compositional profile of an optical fiber with a high sensitivity to strain for strain sensing applications.

2.4 Additive Model

In the thesis a simplified additive model [48] is widely employed for analysis of the doping effect on the acoustic properties of pure silica glass and is applied to the data in order to extrapolate the experimental results to higher dopants concentrations [20]. In particular, the law of mixtures works very well on optical fibers of multiple manufacturers and fabrication

processes. It could result from similar fictive temperatures of rapid glass quenching in the fiber draw process [43].

In the design of these specialty fibers, it is extremely important to know the additive effect on the acoustic velocity (V_A), mass density (ρ), acoustic moduli (M^L), damping coefficient (α), Brillouin spectral width ($\Delta\nu_B$), Brillouin gain coefficient (g_B), refractive index (n_o), and photoelastic constant (Pockels coefficient, p_{12}).

In a well-mixed P_2O_5-doped silica fiber, it is assumed that a fraction value (m) of the total volume is pure P_2O_5, as shown in Figure 2.4. Since two bulk materials are assumed in this system, the (1-m) section accounts for pure silica.

Figure 2.4: A simplified model for a P_2O_5-doped silica fiber. A fraction value (m) of the total volume is pure P_2O_5. A fraction value (1-m) of the total volume is pure silica.

In terms of the physical properties and [P_2O_5] (mol%), the m can be determined as

$$m = \frac{(M_P / M_S)\rho_S[P_2O_5/100]}{\rho_P + [P_2O_5/100]((M_P / M_S)\rho_S - \rho_P)} \qquad (2.8)$$

where m is a volume fraction in a well-mixed glass, [P_2O_5/100] is the mole fraction of phosphorous, ρ_s and ρ_p are the molar masses for silica (s) and phosphorus (p), and M_s and M_p are the molar masses for silica (s) and phosphorus (p).

In order to formulate a model we start with longitudinal modulus (M^L). For this binary system it is assumed that the longitudinal modulus for the mixed glass varies with molar content and is given by

$$M^L = M_P^L + (1 - [P_2O_5/100])(M_S^L - M_P^L) \qquad (2.9)$$

where M^L is the longitudinal modulus. M_S^L and M_P^L are the longitudinal moduli of silica (s) and phosphorus (p), respectively.

For this glass, using Figure 2.4 and m, the average density is determined by

$$\rho = m\rho_P + (1-m)\rho_S \tag{2.10}$$

where ρ (kg/m) is the mass density, and ρ_s and ρ_p are the molar masses for silica (*s*) and phosphorus (*p*), respectively.

Through Equation (2.8), Equation (2.9), and $V_A = \sqrt{M^L/\rho}$ [43], or a determination of a total time-of-flight through the whole segmented fiber in Figure 2.4 [20], the acoustic velocity is found from the following equation:

$$V_A = 1/[m/V_P + (1-m)/V_S] \tag{2.11}$$

where V_A (m/s) is the acoustic velocity. V_s and V_p are the longitudinal velocity of silica (*s*) and phosphorus (*p*), respectively.

Before determining the spectral width as a function of [P_2O_5], one can begin with the determination of an average acoustic damping coefficient in the fiber as a function of acoustic frequency. The average damping coefficient is obtained by summing the attenuation in each segment in Figure 2.4.

$$\alpha(\nu_B) = (\nu_B/\nu_{SMF})^2\left[m\alpha_P(\nu_B) + (1-m)\alpha_S(\nu_B)\right] \tag{2.12}$$

where α (m^{-1}) is the acoustic attenuation coefficient, and α_s and α_p are the acoustic damping coefficient of silica (*s*) and phosphorus (*p*), respectively. In addition, the scaling term (ν_B/ν_{SMF}) accounts for the frequency-squared dependence of the intrinsic linewidth [22], which is proportional to the damping coefficient as seen in Equation (2.12). It is noted that the acoustic frequency is expected to be uniform in a uniform fiber. For a fit to experimental data, a reference value must be selected such that the coefficients α_p and α_s are all the values at a fixed acoustic frequency. In this case the measured acoustic frequency of the L_{01} mode in SMF-28 at 1534 nm is chosen arbitrarily as a reference. Therefore, the coefficients α_p and α_s are all the values at the acoustic frequency 11.008 GHz at 1534 nm.

It is well known that the damping coefficient is related to the Brillouin spectral bandwidth as $\Delta\nu_B = \alpha V_A/\pi$. By Equation (2.11) and Equation (2.12), $\Delta\nu_B$ is related to m, V_s, V_p, α_s, α_p, and ν_B. The relation is re-written as

$$\Delta \nu_B = \frac{(\nu_B / \nu_{SMF})^2 \left[m\alpha_P(\nu_B) + (1-m)\alpha_S(\nu_B) \right]}{\pi \cdot [m/V_P + (1-m)/V_S]}. \qquad (2.13)$$

After gaining $\Delta\nu_B$ from Equation (2.13), the Brillouin gain coefficient (g_B) is determined from the well-known Equation (2.2). It has to be pointed out that g_B does not consider the overlap integral (Γ_m in Eq. (2.1)) between the acoustic and optical waves, so g_B is only for the materials without the waveguide effect. In addition, the modeling of the modal spectral width will be discussed in Chapter 3.

In Equation (2.2), following the same additive method, the refractive index can be obtained using

$$n_o = m \cdot n_P + (1-m) \cdot n_S \qquad (2.14)$$

where n_o is the refractive index, and n_s and n_p are the refractive index of silica (*s*) and phosphorus (*p*), respectively. However, for the optical fiber case, the refractive index should be treated as a modal index considering the waveguide effect. The procedure of obtaining a modal index is first making a six-layer step-wise approximation to the P_2O_5 compositional profile. The additive model is then used to determine the bulk refractive index in each layer using Equation (2.14). A simplified eignvalue method is used to calculate the acoustic modes of the resulting six-layer structure. This gives rise to a modal index of P_2O_5-doped silica fiber. Similarly, one can follow the same procedure to obtain modal acoustic velocity and thus modal acoustic frequency via $\nu_B = 2n_oV_A/\lambda_o$.

It is noted that the Brillouin gain coefficient (g_B) in Equation (2.2) is independent of the optical wavelength for the bulk materials although there may be waveguide effects leading to a wavelength-dependence in an optical fiber. Finally, p_{12} is the remaining unknown in Equation (2.2). The p_{12} values are very similar for several different oxides, but the photoelastic constant of mixed glass can be approximated by the following equation:

$$p_{12} = m \cdot p_{12,P} + (1-m) \cdot p_{12,S} \qquad (2.15)$$

where p_{12} is the acoustic velocity, and $p_{12,s}$ and $p_{12,p}$ are the refractive index of silica (s) and phosphorus (p), respectively. In Chapter 4 the additive model will help determine p_{12} of bulk P_2O_5, which cannot be found in the literature.

The additive model assumes that the glass constituents are independent of each other. Thus, the model can be extended to multiple dopants, for example, three components, GeO_2, B_2O_3, and SiO_2 [49]. In Figure 2.4, the multiple oxide co-dopants D glass including SiO_2 is assumed to be separated into three distinct segments of a unit volume in this model.

Each segment has a pure oxide dopant associated with uniquely intrinsic physical properties described above. The volume fraction m of the dopants is defined by the positions of the interfaces between two segments. More specifically, the volume fractions of components GeO_2, B_2O_3, and SiO_2 are m_1-0, m_2-m_1, 1-m_2, respectively. The m_2 and m_1 can be calculated using the molar fraction, mass density, and molar mass of a constituent oxide. This has to solve a matrix representation for the m_2 and m_1 values. There is an easy way to the express their relation among $[D_i]$, m_i, ρ_i, and M_i using the following equation, where the mole fraction of dopant D_i can be determined,

$$[D_i] = \frac{\frac{(m_i - m_{i-1})\rho_i}{M_i}}{\sum_{i=1}^{3} \frac{(m_i - m_{i-1})\rho_i}{M_i}} \tag{2.16}$$

where m_i is a volume fraction in a well-mixed glass, $[D_i]$ is the mole fraction of dopant D_i, M_i are the molar mass for dopant D_i, ρ_i is the molar density for dopant D_i, and segment i=1,2, or 3 can represent GeO_2, B_2O_3, or SiO_2, respectively.

This equation, in fact, is the same as Equation (2.8), but they use different expressions. After determining the coefficients (m_i) in terms of the dopant compositions, the average acoustic velocity can be found by Equation (2.11) by adding one more term for the third dopant. The new equation means that the average velocity is the unit length divided by the total time-of-flight. Equations (2.9) to (2.15) follow the same method of adding one more term for the third dopant, except for Equation (2.12), which cannot be simplified in this way and has to consider the frequency-dependent acoustic attenuation of boric oxide [14].

The additive model can be also extended to N-1 co-dopants silica [39]. The multiple oxide co-dopants glass is assumed to be separated into N distinct segments of a unit volume in this

model. The mole fraction of dopant D_i can be determined from an equation similar to Equation (2.16) with more terms to represent other dopants. The other equations use the same approach to do so.

Additionally, once the temperature and strain effects on optical fibers are considered in the various physical properties shown in the above equations, they will be explicit functions of the temperature. Meanwhile, these physical properties can be influenced by any residual or induced strain in the fiber. Therefore, new variables, temperature and strain, will be introduced to the equations above [50].

However, the model requires modification in some cases where dopants interact in a non-additive way. A well-known example is the P_2O_5-Al_2O_3 co-doped silica system. Doping P_2O_5 or Al_2O_3 alone into silica increases the refractive index and mass density, but adding P_2O_5 and Al_2O_3 co-doped fiber decreases the refractive index and mass density [51]. It suggests that one would treat the $AlPO_4$ unit cell as an independent species within the additive model.

There are many examples of using the additive model in this thesis. In Chapter 3, the additive model is applied to a six-layer approximation to simulate the Brillouin spectral widths to fit experimental data and thus gain an acoustic attenuation. In order to determine the modal index of optical fiber and P_2O_5-doped silica fiber, the additive model is used to determine the refractive index of each layer in a six-layer approximation and thus obtain modal indices of optical fibers after solving an eigenvalue problem. Following the same procedure, the modal acoustic velocity can be calculated. Using the additive model involving temperature, the TACs of pure silica and bulk P_2O_5 are determined after fitting the experimental data. In Chapter 4, given the SOC of pure silica and the measured SOC P_2O_5-doped silica fiber, the SOC of bulk P_2O_5 can be determined by iterating the SOC values of bulk P_2O_5 until the additive SOC value of P_2O_5-doped silica fiber fits the measured SOC value. Following the same procedure as the determination of TACs, the SACs of pure silica and bulk P_2O_5 are obtained through the additive model.

2.5 Conclusion

The Brillouin scattering introduces the mechanisms of stimulated Brillouin scattering and spontaneous Brillouin scattering and provides comprehensive explanations to link all the optical

and acoustic parameters via mathematics and physics. The background knowledge can help us understand experiments and analysis in the thesis. The dopants and waveguide effect addresses acoustic properties in view of materials and waveguide. The former is related to pure bulk materials in an optical fiber and the latter is about compositional profiles of an optical fiber. Also information is provided about the acoustic and optical properties of several dopants to design specialty fibers. The formulas for temperature and strain effects are elucidated and summarized in this chapter. They will help us understand the thermo- and strain-acoustic properties of optical fibers. They also enables us to design an optical fiber with desirable characteristics using the thermal and strain acoustic properties for applications. The additive model is extremely important to analyze the experimental results for the doping effect on the optical and acoustic properties and to extend the experimental results to higher concentrations for a complete modeling explanation. The equations of all the important physical quantities associated with the additive model have been provided and explained.

The theory and model will be used to explain basic mechanisms, measure important coefficients, and analyze measured data in the thesis.

CHAPTER 3

THERMO-ACOUSTIC EXPERIMENTS

An analysis was presented that began with the measurement of the Brillouin gain spectrum of a heavily germanium-doped optical fiber [19]. From the measured BGS, and a fit to a simple materials model [20] for GeO_2-doped fibers, we were able to extract an acoustic attenuation coefficient of about 1.38×10^5 m^{-1} for bulk GeO_2 at an acoustic frequency of 11 GHz [20]. This value was later revised downward to 1.11×10^5 m^{-1} after a more accurate compositional profile was obtained [21]. This measurement was partly enabled by a large variation in the viscosity profile due to a central burn-out characteristic of fibers manufactured via the modified chemical vapor deposition (MCVD) process. This acoustic attenuation value increases with acoustic-frequency-squared for GeO_2-doped fibers [22]. This data point, in addition to other basic bulk materials parameters, can then be used to calculate and design sets of relevant acoustic profiles for arbitrary compositional profiles and can be extended to include systems of multiple dopants as well.

A similar analysis for a P_2O_5-doped optical fiber will follow; refer to [19] for details such as the model and experimental setups. The present fiber preform is characterized by a similar central index dip, and has fairly sizeable doping (~14.3 mol% oxide at the peak). However, in contrast to the GeO_2-doped fiber studied previously, it is shown that the central burn-out becomes 'filled-in' due to phosphorus diffusion during the fiber draw process. Thus, the test fiber does not contain a significant index dip. It is found that, for the purposes of modeling P_2O_5-doped fibers, including P_2O_5-doped inner cladding layers, bulk phosphorus oxide has an acoustic attenuation coefficient (α_p) of about 1.411×10^5 m^{-1} at an acoustic frequency of 11 GHz. This value is larger than that of bulk GeO_2. Both of these values are approximately 10 times larger than of silica [21]. The spectral width of the L_{01} acoustic mode is found to decrease at a rate of ~ −77.7 kHz/ºC.

Additionally, the results show, for the L_{01} acoustic mode, that the Stokes shift increases at a rate of ~ +0.74 MHz/ºC. Utilizing similar measurements on each of the four observed acoustic modes located in the core, we find the TAC of the bulk P_2O_5 to be about +0.119 m/sec/ºC, less than that of silica. In order to obtain this coefficient from the P_2O_5 and SiO_2 co-doped oxide glass, a pure SiO_2-core (Sumitomo Z Fiber) is first tested in order to obtain the temperature-dependence of the pure silica component. Then, the SiO_2-P_2O_5 system is modeled in an additive way to determine the P_2O_5 TAC. The TAC value for silica, +0.555 m/sec/ºC, is in good agreement with previous measurements on the bulk material [23,24], providing high confidence in the P_2O_5 TAC value. It will also show that each acoustic mode has a unique temperature-dependence of the Brillouin frequency shift due to different spatial distributions.

3.1 Experimental Setup

The experimental configuration described in [19,41] was used to acquire the BGS. Since the pure silica, GeO_2-doped fibers, and the P_2O_5-doped fiber were measured at 1534 nm, the system was Er-doped fiber amplifier-based at 1534 nm. Figure 3.1 is the block diagram of the Er-based experimental configuration.

The Er-based experimental configuration is similar to that in [25]. A continuous wave and external cavity laser diode with less than 100 kHz linewidth works as a 1534nm seed laser. The output light of the seed laser is isolated and then amplified by the first and second Erbium-doped fibers amplifier (EDFA#1 and EDFA#2). The amplified seed signal then passes through Port 2 of an optical circular. The optical circular is produced from SMF-28 fibers and has about 1.5m of this fiber at each of the three ports. Therefore, in addition to the signal from the 3.5-meter fiber under test (FUT), the Brillouin frequency shifts from the SMF-28 fibers were also observed. The amplified seed signal passes into the FUTs with an optical single mode generating the Brillouin scattered signals which propagate back through port 3 of the circulator and into EDFA#3

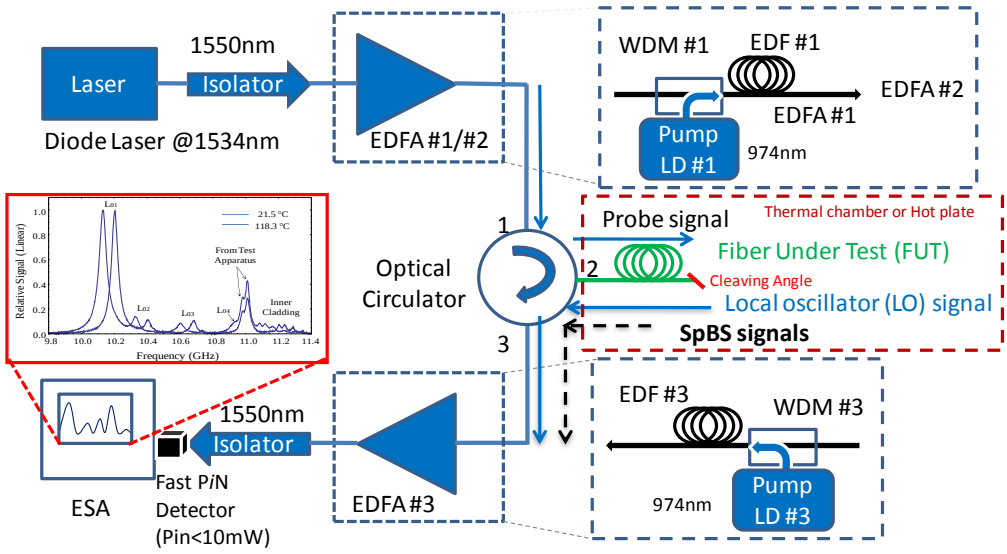

Figure 3.1: Experimental apparatus for temperature measurement of the Brillouin spectrum at 1534nm.

Because of adopting the heterodyne approach, the fundamental local oscillator (LO) signal is required for mixing. The LO signal comes from of a carefully-controlled angled cleave at the output end of the FUT. The Fresnel reflection from the end of the FUT provides an adequate LO signal to achieve low-noise heterodyne detection, but is limited via a cleaving angle so as to not saturate EDFA#3. The Brillouin back-scattered Stokes signals, reflected backward, and a small quantity of pump signal are adequately optically pre-amplified by EDFA#3 operating at a small signal gain before being heterodyned onto a fast P*i*N detector (New Focus 1534). Finally, an Agilent PSA series electrical spectrum analyzer (ESA) captures the resulting spectrum the acoustic modes carried by spontaneous Brillouin scattered signals, and caution was exercised to ensure that Brillouin gain does not narrow the spectra to obscure the measurement. [52].

In addition, the FUT was placed on a hot plate with a temperature controller or inside a thermally-controlled chamber and the calibrated thermometer precisely measured the temperature during measuring the temperature-dependent acoustic parameters of the FUT.

3.2 P_2O_5-Doped Optical Fiber

In the experiments the optical fiber used is one with a P_2O_5-doped silica core fabricated by drawing the corresponding optical preform. The silica fiber preform was fabricated by the MCVD process. A combination of a small MCVD substrate tube, some matched cladding layers, and a large preform core size helped lower the final collapse temperature which maximized the P_2O_5 content in the silica core to 14.3 mol %. The preform was drawn into a cane to reduce the core size. The chemical compositional profiles of the cane were measured by the electron probe microanalysis (EPMA) corresponding to a peak P_2O_5 concentration of roughly 14.3 mol% in the core [25]. The final preform was then drawn into a fiber.

A significant index dip in the central region of the fiber perform core has a significant impact on the analysis. Therefore, the relative index profile (RIP) of the final fiber was measured to determine if this feature was preserved through the draw process. EPMA was not used on the small fiber due to the limited spatial resolution of the available system (~1 μm). The refractive index profile was measured using two methods: the well-known refracted near field (RNF) technique and a high-resolution spatially-resolved Fourier transform technique [53], with measurement wavelengths at 670 nm and 1000 nm, respectively. The results are shown in Figure 3.2.

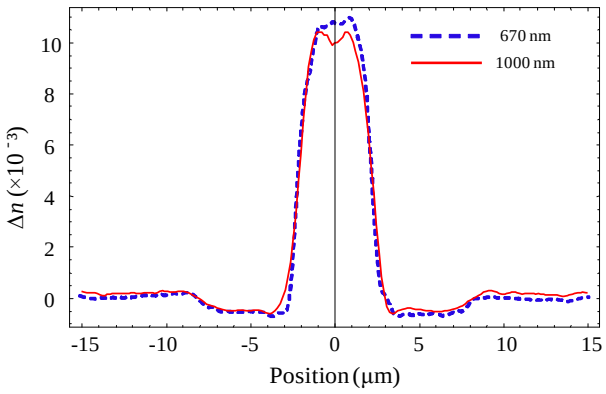

Figure 3.2: Refractive index profile of the final P_2O_5-doped silica fiber measured at 670 nm (dashed line) and 1000 nm (solid line).

The RIP measurements show that the P_2O_5 dopant experienced significant diffusion during the fiber drawing stage. While a slight central dip can be seen in the 1000 nm high-resolution

data, the large burnout observed appears to have been completely filled in. In addition, a slight decrease in the refractive index difference is observed in going from 670 nm to 1000 nm, which can be attributed to either chromatic dispersion of the P_2O_5 dopant or a slight variation in the dopant concentration between the two measurement samples.

The RIP measurements of the fiber obtain the dopant concentration in the core and the results were found in [54]. Due to the proximity of the wavelength of the York system (632 nm) to that of the RNF method employed here (670 nm), the RNF data was used to determine the P_2O_5 concentration in mol%. Therefore, based on the measured RIP, [P_2O_5] in the center of the fiber is 12.2 mol%. This finding supports the conclusion that the fiber of the present study does not possess a central dip since P_2O_5 diffused into this region during the drawing process. Finally, since our Brillouin scattering measurements are performed at 1534 nm (λ_o), it is assumed that the RIP measurement at 1000 nm is a good approximation to the RIP at 1534 nm, and thus from this data the optical mode can be calculated. Finally, since our Brillouin scattering measurements are performed at 1534 nm (λ_o), it is assumed that the RIP measurement at 1000 nm is a good approximation to the RIP at 1534 nm, and thus the optical mode can be calculated from this data.

3.3 Room Temperature Measurements

3.3.1 Brillouin gain spectrum

The measured BGS of the P_2O_5-doped fiber is shown in Figure 3.3. A total of eleven acoustic modes were observed. Four peaks (L_{01} to L_{04}) can be attributed to modes that reside primarily in the core of the test fiber. Two modes (L_{05} and L_{06}) around 11 GHz are from the optical circulator in the test apparatus including a Corning SMF-28 leader attached to the circulator fiber. The remaining five peaks (L_{05} to L_{09}) result from acoustic modes residing primarily in the matched-index deposited inner cladding. A best-fit consisting of a summation of eleven Lorentzian profiles was performed, with the results of the measured values summarized in Table 3.1.

The measured spectra with two different temperatures also are shown in Figure 3.3 when only the P_2O_5-doped fiber was heated from room temperature (21.5 ºC) to a higher temperature

(118.3 ºC). Much as is observed with GeO_2-doped fibers [28], the spectrum narrows and the Stokes frequency increases with increasing temperature. The fibers associated with the measurement apparatus were not heated. Therefore, these peaks are fixed in frequency as indicated by Figure 3.3 while the test fiber was heated. Additionally, the L_{04} mode almost merges into the peak of the test apparatus at 21.5 ºC due to the relative strength and position of this peak. At 118.3 ºC the L_{04} mode becomes hidden underneath the peaks of the test apparatus due to an increasing frequency shift with increasing temperature. Even though the peaks of the test apparatus get smaller, the L_{04} mode is essentially invisible under them. This also introduces increased measurement error for the L_{04} mode at elevated temperatures.

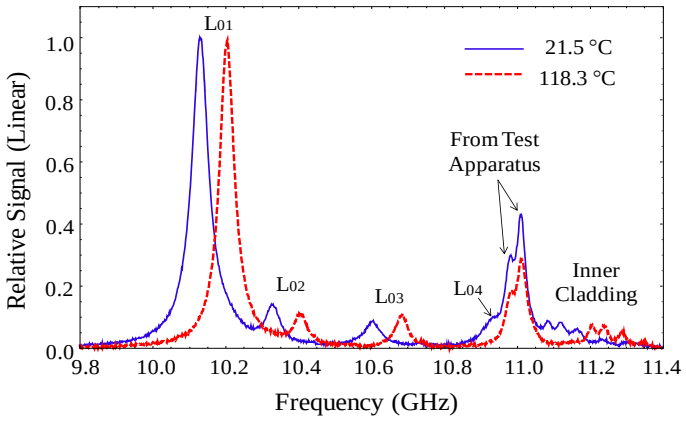

Figure 3.3: Brillouin spectrum of a 3.5 m segment of the P_2O_5-doped optical fiber at 1534 nm and at two different temperatures, 21.5°C and 118.3°C. Four acoustic modes primarily located in the core are observed, while five reside mainly in the inner cladding. The two peaks near 11 GHz are due to the measurement apparatus.

3.3.2 Acoustic velocity and attenuation coefficient

A fit to the data was performed using a model in much the same way as found in [19]. In this present case, a six-layer step-wise approximation was made to the RIP of the P_2O_5-doped fiber. The first four layers correspond to the core, one to the inner cladding, and one to the outer pure silica cladding. The velocity of the deposited inner cladding was deduced from the measured data since it had a fairly complicated profile owing to the deposited MCVD layers and presence of fluorine. To formulate the fit, the approximate compositional profile (the second column in Table 3.2) was first determined with the help of the data in Figure 3.2 based on a linear

relationship between $[P_2O_5]$ and Δn with a maximum difference of about 6% over the range $0 < [P_2O_5] < 15$ mol% between the addition model and its linear fit [25]. Then, invoking the materials model in [20], here $V_L = 1/[m/V_p + (1-m)/V_s]$ and $\alpha(\nu_B) = m\alpha_p(\nu_B) + (1-m)\alpha_s(\nu_B)$ are used to calculate the bulk values in each layer, with the acoustic velocity (V_p and V_s) and attenuation coefficients (α_p and α_s) for the bulk materials (P_2O_5 and SiO_2) used as fit parameters. More specifically, these values were iterated until the differences between the measured and calculated modal frequencies (columns 2 and 3 in Table 3.1, respectively) and spectral widths (columns 4 and 5 in Table 3.1, respectively) were minimized for all modes simultaneously. Given the close proximity of the modeled and measured modal frequencies, there is more confidence in our assignment of the acoustic modes.

Table 3.1: Measured parameters for all observed acoustic modes *m*.

Mode m	*Measured* ν_m (GHz)	*Modeled* ν_m * (GHz)	*Measured* $\Delta\nu_m$ (MHz)	*Modeled* $\Delta\nu_m$ ** (MHz)	*Relative Amplitude*	*Designation*
1	10.131	10.116	56.5	56.7	.999	L_{01}
2	10.330	10.342	49.0	56.7	.117	L_{02}
3	10.604	10.620	57.0	57.3	.077	L_{03}
4	10.931	10.929	56.0	55.7	.060	L_{04}
5	10.980	-	30.0	-	.202	L_{01}***
6	11.012	-	30.5	-	.379	L_{01}***
7	11.086	-	26.5	-	.053	L_{05}
8	11.121	-	28.5	-	.056	L_{06}
9	11.166	-	40.0	-	.044	L_{07}
10	11.236	-	24.0	-	.017	L_{08}
11	11.305	-	30.5	-	.013	L_{09}

* The modeled values after tweaking V_P fall within 0.16% of the measured values.
** The modeled values after tweaking α_P fall within 0.58% of the measured values except for L_{02}.
*** Due to the measurement apparatus (circulator).

The results of this fit are shown in Table 3.2 for the bulk materials, as well as the resulting values for each of the layers. Here, V_L is the longitudinal acoustic velocity, V_S is the shear acoustic velocity, $\Delta\nu_B$ is the Brillouin spectral width, ρ is the mass density, and Δn is the refractive index difference. Since the fifth layer has a very small amount of fluorine to make this

layer a matched-index cladding (fluorine reduces the acoustic velocity), the measured acoustic velocity value is used via the fundamental cladding mode frequency (L_{05}) and $v_{L05}=2V_m n_{modal}/\lambda_o$ (V_m is modal acoustic velocity of L_{05}, n_{modal} is modal index of the optical mode in the P_2O_5-doped fiber, and λ_o is optical wavelength). Additionally, the bulk acoustic velocity has a nonlinear, monotonically decreasing relationship with increasing P_2O_5 concentration (mol%). For a very small range of concentrations one can assume that the curve is approximately linear (−0.90%/mol%) up to 10mol % [25].

Table 3.2: Approximation (best-fit) to the profile provided in Figure 3.2.

Layer	$[P_2O_5]$ (mol%)	V_L (m/s)	V_S (m/s)	$\Delta\nu_B$ (MHz) (@ L_{01} Mode)	ρ (kg/m^3)	Δn^* (10^{-3})	a (μm)
1	12.2	5331	3348	57.5	2244	10.2	1.15
2	11.0	5380	3381	53.7	2240	9.3	1.70
3	8.3	5501	3458	44.6	2231	7.3	2.20
4	3.5	5751	3616	27.1	2214	3.2	2.50
5**	2.0	5843	3673	21.1	2208	1.9	8.00
6	0	5970	3749	13.0	2200	0	∞
SiO_2	0	5970	3749	17.0 *** [21]	2200	0	-
P_2O_5	100	3936	2471	176.8 ***	2390	44	-

* The bulk refractive index of silica is assumed to be 1.443 at 1534 nm.
** Assuming no fluorine. V_L=5882m/s and V_S=3698m/s, ρ=2200kg/m^3, and Δn= − 0.0005 used in the simulation is due to the presence of fluorine.
*** Bulk value at 11GHz.

The modeled Stokes shifts and Brillouin spectral widths are shown in Table 3.1 in order to compare with the measured data. The largest error in the Brillouin spectral width is for the L_{02} mode. The difference in the Stokes shift for this mode, 12MHz, corresponds to about 6.21 m/s, which is roughly 1.27% of the difference between the L_{02} modal velocity and that of bulk silica. The uncertainties of the measured Brillouin spectral widths for the L_{01}, L_{02}, L_{03}, and L_{04} modes are ±0.5MHz, ±1.0MHz, ±1.0MHz, and ±3.0MHz, respectively. As described above, because the L_{04} mode is close to the peaks of the test apparatus, their overlapping nature introduces more spectral width uncertainty for this mode.

The spectral width of each mode was modeled using the following expression [21]:

$$\Delta\nu_m = \int_0^\infty \Delta\nu_B(\nu_m, r)\,u(r)\,u^*(r)\,r\,dr \qquad (3.1)$$

where $\Delta\nu_B$ (ν_m , r) is the bulk spectral width at the modal frequency ν_m at the spatial position r, and $u(r)$ is the power-normalized acoustic displacement, which is dependent on the acoustic mode. Equation (3.1) essentially represents an average spectral width, weighted by the power distribution of the acoustic mode within the dynamic viscosity profile. Details on how the acoustic mode was calculated, using a simplified eigenvalue problem, are also provided in [19].

The fitted spectral widths provided in Table 3.2 for each layer are listed utilizing the L_{01} parameters. In particular, the modal acoustic velocity with the optical modal index to define the acoustic mode frequency is used in $\Delta\nu_m = \alpha V_m/\pi$ with $V_m = \nu_m\lambda_o/2n_{\text{modal}}$ and $\alpha \propto \nu^2_m$. Since these modal values are different for the higher-order acoustic modes, these spectral widths are also different for each mode. The L_{01} parameters provide a point-of-reference from which the spectral widths of the other modes can be calculated by invoking the frequency-squared dependence of the Brillouin spectral width.

Since the Brillouin spectral width of the fiber of this study decreases with increasing temperature, it has been assumed that the spectral width of P_2O_5-doped silica fibers obeys the simple frequency-squared law ($\Delta\nu_m \propto \alpha \propto \nu^2_m$), in contrast to some materials such as B_2O_3-doped germanosilicate optical fibers [14]. These effects were taken into consideration for the final fit. Therefore, in Table 3.2 the best-fit spectral width (177 MHz at 11 GHz) for phosphorus oxide is the bulk-material value. This corresponds to an acoustic attenuation coefficient of about 1.411×10^5 m^{-1} at 11 GHz. This frequency was previously taken as a convenient reference since it is the Brillouin frequency shift of the L_{01} acoustic mode of Corning SMF-28 at 1534 nm.

3.3.3 Spectral width vs. mode number

As with the GeO_2-doped fiber of [19], the spectral width decreases with increasing mode number. In [19], this resulted from the fact that the proportion of acoustic power occupying the inner dip region of the core increases as the mode number increases. The other fact that the central dip region in the GeO_2 fiber contained a lower GeO_2 concentration with a larger acoustic

attenuation coefficient than SiO_2 leads to narrower Brillouin spectra for modes occupying a greater proportion of that region.

However, in the present case the P_2O_5 concentration proportional to Δn in Figure 3.2 is decreasing radially outward in the region between 1 and 3 μm. Since the inner-core region has more P_2O_5 and less SiO_2 than the outer-core region, and since SiO_2 has a much lower attenuation coefficient than P_2O_5, the spectral widths of the higher-order acoustic modes (HOAMs) are smaller than that of the fundamental mode. This results from the increasing mode diameter of the HOAMs with increasing mode number. The fundamental acoustic mode is most tightly confined to the center of the fiber where the acoustic attenuation is the largest. To illustrate this point, Figure 3.4 shows a plot of normalized longitudinal acoustic modes L_{01} and L_{04} together with the measured RIP.

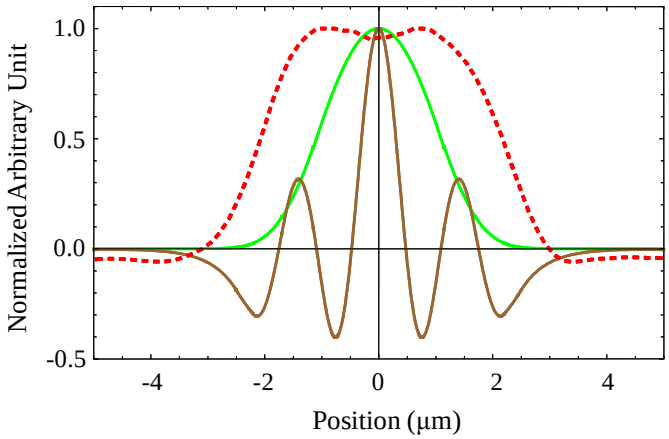

Figure 3.4: Normalized longitudinal acoustic modes L_{01} and L_{04} with the measured RIP. The red-dashed curve is the RIP. The green curve is the spatial distribution of L_{01} and the brown curve is the spatial distribution of L_{04}. The spatial distribution of L_{04} has a bigger mode diameter than that of L_{01} and occupies more of the outer-core region.

3.4 Temperature-Dependent Measurements

3.4.1 Acoustic frequency and spectral width vs. temperature

It is important to understand how temperature influences the acoustic properties of the P_2O_5 fiber at higher temperatures. Figure 3.3 shows the differences in the Brillouin gain spectrum between 21.5°C and 118.3°C for all acoustic modes in the core and cladding of the fiber. Figure 3.5 investigates the spectral widths and frequency shifts of the fundamental mode (L_{01}) over the measured temperature range. In Figure 3.5 the trends are both approximately linear, with the Stokes shift increasing at a rate of ~ +0.74 MHz/ºC and the spectral width decreasing at a rate of ~ −77.7 kHz/ºC. Interestingly, in Figure 3.3 the inner cladding has a Stokes shift rate of ~1.22MHz/ºC that is larger than that in the core of the fiber. This can mainly be attributed to the fact that the inner cladding is lightly doped.

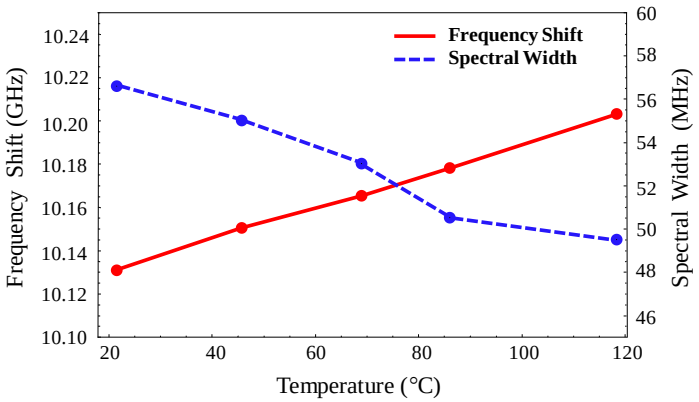

Figure 3.5: The trends are both approximately linear in the available measurement range, with the Stokes shift increasing at a rate of ~ +0.74 MHz/ºC and the spectral width decreasing at a rate of ~ −77.7 kHz/ºC for the main mode.

The HOAMs in the core at different temperatures are studied by following the modeling method of Section 3.3 to investigate the temperature dependency of the Stokes shift of all the acoustic modes in the core. To first order, it is only considered that the acoustic velocity and refractive index are temperature-dependent. Other relevant quantities (namely the mass density) are assumed to be negligibly dependent on the temperature. Referring to Table 3.2, this means

that the values in columns 3, 4, and 7 vary with the temperature, and this gives rise to a temperature-dependence of the calculated Stokes shift and modal index through the relation, $V_m(T) = v_m(T)\lambda_o/2n_{\text{modal}}(T)$.

3.4.2 Thermo-optic coefficient

Since the P_2O_5 concentration is different for each layer, each layer will have a unique TAC and TOC. The unique TAC and TOC of bulk P_2O_5 can be determined through the room temperature method in section 3.2.2 involving temperature. For bulk materials, once given is its TOC value, its TAC value can be determined.

The temperature-dependent Sellmeier model [55] provides the refractive index of bulk pure silica and its refractive index at 21.5 ºC is offset to 1.443 in accordance with the Table 3.2 assumption. With the refractive index of bulk P_2O_5 found in Table 3.2 and using the TOC (-9.22×10^{-5}/ºC) found in [29,56], one can gain the refractive index of P_2O_5 at different temperatures and different concentrations for simulating the P_2O_5-SiO_2 mixture via the additive model. In addition, it is assumed that the thermo-optic effect of phosphorus dominates fluorine in the fifth layer in Table 3.2 at higher temperatures due to the insignificant thermo-optic effect of fluorine in a silica glass with very low concentration as in the present case [57]. Then, from the data, one can deduce an analogous TAC for the acoustic velocity.

3.4.3 Thermo-acoustic coefficient

3.4.3.1 TAC of pure silica optical fiber

To model the acoustic velocities, it is first assumed that the bulk acoustic velocity of both P_2O_5 and SiO_2 are linearly related to the temperature over a small temperature range. For P_2O_5 one can write

$$V_A^{P_2O_5}(T) = C_p\left(T - 21.5^{\circ}\text{C}\right) + 3936.00\text{m/s} \qquad (3.2)$$

where C_p is a constant (units of m/s/ºC).

Additionally, a similar temperature-dependent linear equation of acoustic velocity for SiO_2 is extracted from measurements of frequency vs. temperature on a commercial pure silica core fiber (Sumitomo Z Fiber). Figure 3.6 shows the best linear fit to the measured Brillouin frequency shift of the Z Fiber as a function of temperature.

Using the calculated temperature-dependent modal index [55] for the Z Fiber, this linear equation is converted to obtain the temperature-dependent linear equation of acoustic velocity as

$$V_A^{SiO_2}(T) = 0.555\left(T - 21.5^{o}\mathrm{C}\right) + 5968.65\mathrm{m/s}. \qquad (3.3)$$

It is well known that the fundamental mode of the Z Fiber dominates the Brillouin gain spectrum, and the acoustic and optical index profiles of the Z Fiber in the core are almost uniform. Furthermore, the calculations indicate that the fundamental acoustic mode velocity is very similar to the value of the core material, and thus we assume that its modal acoustic velocity can represent the acoustic velocity of bulk pure silica (core material) without introducing significant error. The slope found here, +0.555 m/sec/ºC, is in good agreement with previous measurements on the bulk material over our measured temperature range [23,24], providing a high degree of confidence in Equation (3.3).

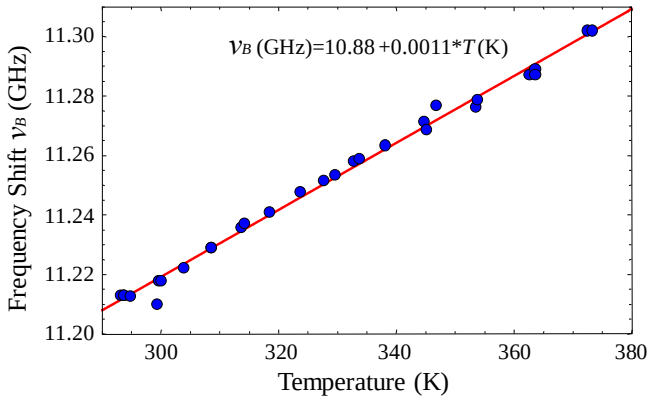

Figure 3.6: The linear equation for the frequency shift of Z Fiber as a function of fiber temperature as a best fit to the measured data. This linear equation is used to obtain the temperature-dependent acoustic velocity of SiO_2.

We have to indicate that the P_2O_5-doped fiber and the Z Fiber are produced by different manufacturers with different conditions. It is therefore not surprising that the room temperature acoustic velocity of pure bulk silica derived from the Sumitomo fiber (5969 m/s) differs slightly

from that provided in Table 3.2 (5970 m/s). This may be due to different thermal histories [58] or draw tensions [59]. For consistency with the present analysis, the interception in Equation (3.3) of the linear equation of the acoustic velocity is offset to 5970 m/s for the temperature-dependent acoustic velocity of SiO_2.

3.4.3.2 TAC of P_2O_5-doped optical fiber

To perform a best-fit to measured data is to determine C_p in Equation (3.2), each acoustic mode is calculated using the temperature-dependent six-layer approximation. Table 3.2 shows room temperature values, with each layer possessing a unique TAC and TOC. C_p is iterated until the error across all acoustic modes is minimized. While C_p is the only remaining unknown here, fitting simultaneously to all four acoustic modes increases the confidence in the determined value and leads to interesting physical conclusions.

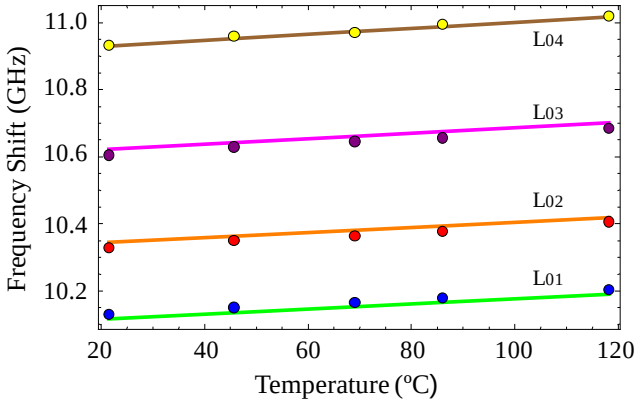

Figure 3.7: The modeled frequency shift (solid line) and the measured frequency shift (circle) vs. temperature. All the trends are approximately linear in the available measurement range. The modeled data of each of the modes are very close to the measured points.

The result of Brillouin frequency vs. temperature is shown in Figure 3.7, where the solid lines correspond to the modeled data and the circles to the measured data. Figure 3.7 shows that modes 1, 2, 3, and 4 have maximum errors 0.161%, 0.150%, 0.156%, and 0.078% in the acoustic frequencies, respectively. The slight error in frequency may be attributable to uncertainty in the dopant profile.

Table 3.3: The comparison of measured and modeled linear equations of the temperature-dependent frequency shift

Mode	Measured $v_m(T)$ (GHz)	Modeled $v_m(T)$ (GHz)	Designation
1	$0.7351 \times 10^{-3}\,T + 10.115$ R^2=0.9988291	$0.7562 \times 10^{-3}\,T + 10.100$ R^2=1.0000000	L_{01}
2	$0.7737 \times 10^{-3}\,T + 10.312$ R^2=0.9969427	$0.7865 \times 10^{-3}\,T + 10.325$ R^2=1.0000000	L_{02}
3	$0.8168 \times 10^{-3}\,T + 10.588$ R^2=0.9976847	$0.8240 \times 10^{-3}\,T + 10.602$ R^2=0.9999997	L_{03}
4	$0.9150 \times 10^{-3}\,T + 10.913$ R^2=0.9868277	$0.8874 \times 10^{-3}\,T + 10.910$ R^2=0.9999744	L_{04}

Table 3.3 provides the temperature-dependent linear equations of measured and modeled frequency shifts for the first four modes. The best-fit value for C_p is found to be +0.119 m/sec/ºC. Utilizing this value, the measured and modeled slopes of the frequency versus temperature curves are all within 3.02% of each other, indicating that this is a very good fit to data.

It is interesting that the slope of the temperature curves is increasing with increasing mode number. As with the spectral width, since the HOAMs occupy proportionally more space in the outer region of the core than the fundamental mode, where there is less P_2O_5, the slope is expected to increase with increasing mode number. This is because the acoustic velocity of silica has a larger dependence on temperature than P_2O_5, as seen by comparing Equation (3.3) given that C_s= +0.555 m/sec/ºC and Equation (3.2) given that C_p= +0.119 m/sec/ºC, and because P_2O_5 has a relatively large negative thermo-optic coefficient (-9.22×10^{-5}/ºC) while SiO_2 has a positive thermo-optic coefficient (1.065×10^{-5}/ºC at 1534nm) [55].

3.5 Conclusion

Through BGS measurements of a fiber with high P_2O_5 content in the core, an acoustic damping coefficient for bulk P_2O_5 is provided. It is suitable for modeling purposes. It is found that this

coefficient is about 1.411×10^5 m^{-1}, which is larger than that of GeO_2. The results for the effect of phosphorus oxide on the longitudinal velocity (~ −0.90%/mol% up to 10mol%) are similar to those (~ −0.71%/mol% up to 5.5mol%) found in [18]. It has been found that the temperature coefficients for the Stokes frequency shift and Brillouin spectral width for the L_{01} acoustic mode of the fiber are ~ +0.74 MHz/ºC and ~ −77.7 kHz/ºC, respectively. The thermo-acoustic coefficient of bulk P_2O_5 is determined to be about +0.119 m/sec/ºC, which is much lower than that of pure silica (+0.555 m/sec/ºC). It has been shown that these bulk coefficients can be used to predict the temperature-dependent Stokes shift of the higher-order acoustic modes with a high degree of accuracy. This data is also useful for the design of acoustic profiles of optical fiber for applications where Brillouin scattering is significant.

CHAPTER 4

STRAIN-ACOUSTIC EXPERIMENTS

Chapter 3 presented an analysis utilizing a simple materials model [20] fitted to a series of measurements of the Brillouin gain spectrum of a heavily P_2O_5-doped fiber. The results provide the acoustic velocity (V_A), acoustic attenuation (α), and thermo-acoustic coefficient (C_p) of bulk P_2O_5. These values can be used to calculate and frame sets of designer acoustic profiles for specialty fibers with arbitrary compositional profiles, and can be extended to include systems of multiple dopants for distributed temperature sensing applications.

For completeness, a similar analysis is presented in this chapter for the tensile strain effect on the same P_2O_5-doped optical fiber. Reference [25] provided details such as models, fiber characteristics, and experimental setups for measurements of the BGS. A strain-optic coefficient and strain-acoustic coefficient for bulk P_2O_5 derived and presented in this chapter can be utilized in designing specialty fibers for distributed strain sensing applications.

It is well known that the dependence of the Brillouin frequency (v_B) on optical wavelength, acoustic velocity, and refractive index is given by $v_B = 2V_A n_{\text{modal}} / \lambda_o$, where V_A is acoustic velocity of acoustic mode, n_{modal} is modal index of the optical mode in the fiber, and λ_o is optical wavelength. To first order, we assume that only the acoustic velocity and refractive index are strain-dependent. The change in the refractive index as a function of induced strain is proportional to SOC and it is convenient to define $\text{SOC}=p_{12}-\sigma\cdot(p_{11}+p_{12})$ here [36]. The coefficient can be calculated from the Pockels coefficients (p_{11} and p_{12}), the Poisson ratio (σ), and the zero-strain refractive index (n_o).

Despite an extensive literature search, the SOC of bulk P_2O_5 was not reported in the literature while the SOC values of bulk SiO_2 were well known. This can be attributed to the difficulty in working with the bulk material due to its being highly hygroscopic [60]. On the other hand, the SOC values of bulk SiO_2 and silica fiber were reported and thus SOC=0.1936 if p_{11}=0.113, p_{12}=0.252, σ=0.16 [27].

However, a known SOC of bulk P_2O_5 can determine its SAC, as in the previous work [25]. Therefore, in order to obtain the SAC of bulk P_2O_5 from the P_2O_5 and SiO_2 co-doped oxide glass, a pure SiO_2-core (Sumitomo Z Fiber) and heavily-P_2O_5-doped silica fiber were first tested to obtain the SOC values of the pure silica component (SiO_2) and composite silica (P_2O_5-SiO_2) fiber utilizing the strain-dependent free spectral range of a fiber ring laser [31,32] that is constructed utilizing a segment of this fiber. The SOC values of P_2O_5-doped silica fiber and pure silica fiber (Z Fiber) are obtained to be 0.189 and 0.194, respectively. From these values the bulk P_2O_5 SOC can be deduced through an additive model [20]. It is found that the SOC of bulk P_2O_5 are ~ +0.139 which is lower than the pure silica value. The SOC for a Sumitomo Z Fiber (pure silica core and F-doped cladding) is in good agreement with previous measurements on the pure silica fiber [27], providing a large degree of confidence for our formalism in the P_2O_5 SOC value (= $dn/d\varepsilon$). Then, measurements of the BGS at various strains enable a determination of the SAC (= $dV_A/d\varepsilon$).

In addition, utilizing Brillouin gain measurements of P_2O_5-doped fiber and the measured SOC for bulk P_2O_5, the Pockels coefficients (photoelastic coefficients, p_{11} and p_{12}) are estimated. It is suggested that the p_{12} values of bulk pure silica and P_2O_5 are approximately equivalent [36]. Although this estimate may have considerable error associated with it, to the best of our knowledge, this is believed to be the first attempt at elucidating these values for P_2O_5. The p_{12} value could further extract p_{11} from the SOC of bulk P_2O_5 using a well-known Poisson ratio of bulk P_2O_5 [33] in an additive way.

Finally, from measurements of the Stokes frequency shift with strain changes, the results show that, for the L_{01} acoustic mode, the Stokes shift increases approximately linearly with elongation at a rate of ~ +407.26 MHz/1% and +505.93 MHz/1% for P_2O_5-doped silica fiber and SMF-28, respectively. While the rate of standard GeO_2-doped SMF-28 fiber is higher, both of these values are less than that 524.66 MHz/1% of pure silica fiber (Z Fiber). It is found to be much less dependent on strain in P_2O_5 than in SMF-28 and in pure silica fiber as well.

The SiO_2-P_2O_5 system is modeled in an additive way to determine the P_2O_5 SAC value. Utilizing these SOC coefficients of bulk P_2O_5 and pure silica and the measurement data on each of the four observed acoustic modes located in the core in the same additive way as done previously [25], the modeled and unique slopes of the Stokes-shift-versus-strain curves for the four observed acoustic modes each lie within 1.974% of the measured values. Thereby through

the relation of acoustic velocity versus strain, it is found that the SAC of bulk P_2O_5, is about +9854 m/s/ε, which is much less than that of bulk SiO_2, ~ +29240 m/s/ε, found in our measurements.

4.1 Experimental Setup

4.1.1 Strain-optic coefficient measurement

As previously stated, extensive literature searches were unsuccessful in finding an SOC appropriate for bulk P_2O_5. Thus, instead measurements on the P_2O_5 fiber are relied on to determine this value. Both time-of-flight and Mach-Zehnder configurations were considered, but both required precision control and measurements that could not be achieved with our experimental setup. Therefore, utilizing the fiber ring-based strain sensor [31,32] as the apparatus can measure the SOC of the P_2O_5-doped fiber. In the experimental configuration, the test fiber becomes part of the laser cavity, and any strain imparted on this fiber will result in a change in the cavity free-spectral range. The change in FSR can be connected to the strain-induced change in fiber length and refractive index, which would determine the relation of strain vs. refractive index.

The experimental apparatus for strain-optic coefficient measurements is shown in Figure 4.1. A fiber ring laser is constructed from a commercial erbium-doped fiber amplifier (JDSU MicroAmp) that serves as the gain block, and a tap coupler that serves as the output port and feedback mechanism. Unidirectional laser operation is ensured by isolators built into the EDFA. There is no attempt to otherwise stabilize the cavity since the presence of a large number of cavity modes is a desirable laser attribute to detect the strain-induced change with a higher accuracy. Incorporating the test fiber into the laser cavity is made by splicing FC/APC-connectors as pigtails to its ends. The output of the laser is sent directly to a P*i*N detector (New Focus 1534) and then the spectrum of the resulting beat signal is measured with an electrical spectrum analyzer (Agilent 8560). The beat frequencies measured by the ESA represent the cavity mode spacing (FSR) and its harmonics resulting from the presence of multiple evenly-

spaced cavity modes. Then, a strain on the P_2O_5-doped fiber under test results in a change in FSR that is observed as a frequency shift at the ESA. The SOC can be easily determined from the change in FSR as a function of strain.

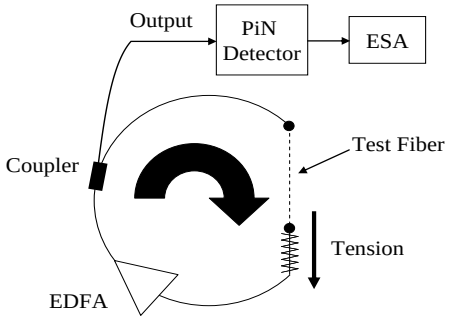

Figure 4.1: Experimental apparatus that is used to measure the SOC. The test fiber becomes part of the ring laser and any strain results in a measurable change in the cavity FSR.

4.1.2 Estimate of the Pockels coefficients

Figure 4.2 shows a block diagram of the experimental apparatus used to measure the Brillouin gain coefficient (g_B) utilizing stimulated Brillouin scattering.

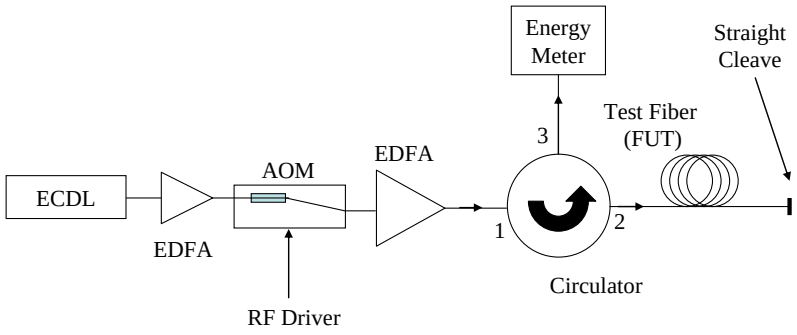

Figure 4.2: Experimental setup used to measure the Brillouin gain coefficient.

It is well known that g_B can be used to estimate p_{12}. This will be described later. The experimental setup starts with a narrow-linewidth external-cavity diode laser (ECDL) (1550 nm) seed source that is pre-amplified in the first EDFA. The signal passes through a fiber-coupled acousto-optic modulator (AOM) and is pulse-amplified by the second EDFA. The output of the second EDFA is then sent into port 1 of a circulator. Then, the signal is launched into the fiber

under test via port 2. Any scattered light passes back through the circulator and emerges from port 3, and then into a pulse-energy meter. An adequate pulse length of 347ns is utilized in the measurements to match the fiber length. It is obvious that pulses shorter than this value result in a reduced effective SBS interaction length which decreases the Brillouin gain [1]. On the other hand, pulses much longer than this were found to have a considerably altered shape such that much of the pulse does not contribute to the SBS process [61].

4.1.3 Strain-acoustic frequency measurements

The experimental configuration in Figure 4.3 used to acquire the BGS is identical to that described in [36,32], except that the fiber is under tension described later. In short, the BGS is measured utilizing spontaneous Brillouin scattering with the fiber under test spliced to the output of the measurement system. In the measurement system, a continuous-wave, narrow-linewidth (<100kHz) external-cavity laser diode signal is amplified and passes through a circulator to a test fiber. Then, the back-scattered Stokes signal and a small quantity of pump signal (courtesy of a carefully-controlled angled cleave at the test fiber output) propagate back through the third port of the circulator, are optically pre-amplified, and finally heterodyned onto a fast P*i*N detector and the resulting spectrum is captured with an electronic spectrum analyzer. Caution was exercised to ensure that Brillouin gain did not narrow the spectra and obscure the measurements [52].

For the fiber-under test portion, the strain effect on the P_2O_5 fiber is measured and the SMF-28 fiber is considered as a reference fiber. Prepared were samples including a P_2O_5 fiber, a SMF-28 fiber, and a pure silica fiber (Z Fiber) with 99.0cm, 82.2cm, and 271.6cm in length, respectively. The output end of the FUT is secured to a metal plate via an epoxy and the other end is attached to a linear translation stage with a strain-gauge. These samples are applied by the different tensions from 120g to 720g, from 500g to 900g, and from 180g to 660g, respectively. A linear strain is then applied to the whole length of fiber. In the mean time, The BGS is measured to gain the Stokes frequency shifts up to around 1% elongation (linear and elastic region) at 1534nm. After the length increments under different tensions are gained and elongations (tensile strain) are calculated and calibrated, one can calculate the linear equation of the tension as a function of the length increment within elastic range governed by Hooke's law.

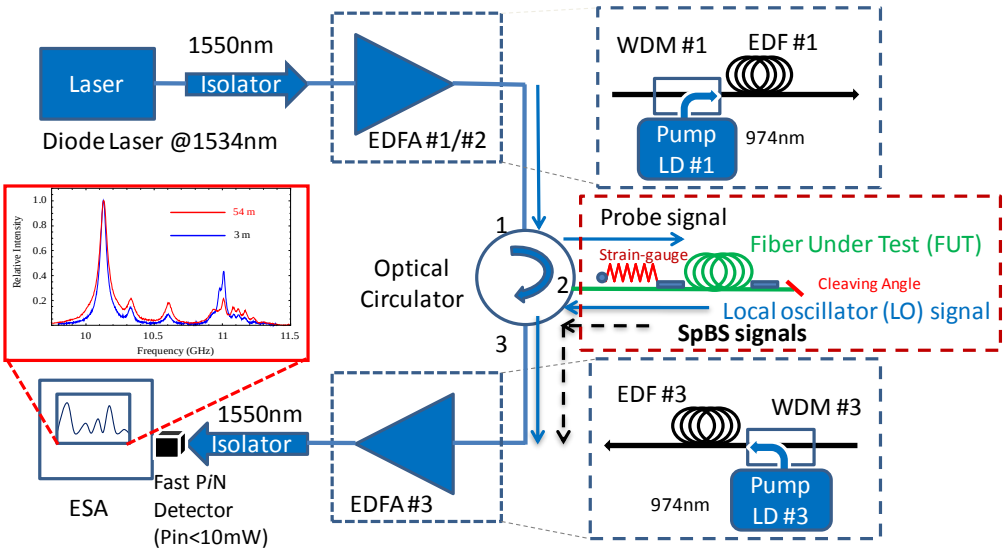

Figure 4.3: Experimental apparatus for strain measurement of the Brillouin spectrum at 1534nm.

4.2 P_2O_5-Doped Optical Fiber

Referring to section 3.2, the optical fiber used in this set of experiments is one with a heavily P_2O_5-doped silica core fabricated by the modified chemical vapor deposition process at INO of Canada. The core glass of the resulting fabricated fiber is in amorphous state, while the additive model averages any local structure in the P_2O_5 dopant into net values of bulk P_2O_5. Detailed information regarding its refractive index and compositional profiles is given in [25]. In short, based on the measured refractive index profile, the P_2O_5 concentration in the center of the fiber is approximately 12.2 mol%. This finding supports the conclusion that the fiber of the present study does not possess an index dip since P_2O_5 diffused into this region during the drawing process.

4.3 Strain-Optic Coefficient

4.3.1 Free spectral range

The fiber ring-based strain sensor as reported in [31,32] can be used to measure the SOC of the P_2O_5-doped fiber. The FSR of a unidirectional traveling-wave ring laser is well known to be

$$\Delta\nu = FSR = \frac{c}{nl} \tag{4.1}$$

where n is the modal refractive index and l is the cavity length. Figure 4.4 shows the free spectral range and its harmonics due to the presence of multiple even-space cavity modes. It is worth pointing out that the light wave travels one way as shown in Figure 4.1. Therefore, there is one time of l in the denominator of Equation (4.1).

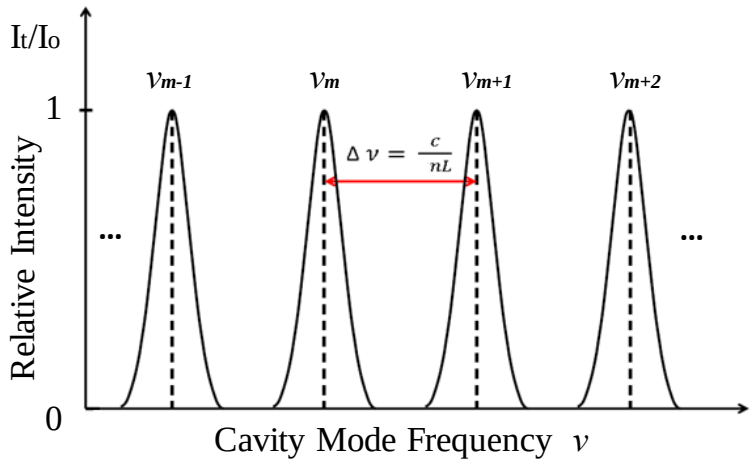

Figure 4.4: The beat frequencies ($\Delta\nu$) measured by the ESA (ν_{ESA}) represent the cavity mode spacing (=*FSR*) and its harmonics resulting from the presence of multiple evenly-spaced cavity modes.

It is assumed that the refractive index has the linear form $n = n_o + \varepsilon \cdot Q$. Similarly, the length has the form of $l = l_o + \varepsilon \cdot l_o$. The subscript '$o$' represents the zero-strain values. Unless otherwise stated as a percentage (%), throughout this paper the strain ε is taken as a fractional elongation. Since only a small portion of the ring laser experiences strain, in order to explicitly contain

contributions from both the unstrained and strained fiber components, the FSR can be rewritten as

$$FSR = \frac{c}{nl + NL}. \tag{4.2}$$

Here, *nl* is contributed from the segment of fiber that will be strained, and *NL* is due to the remainder of the ring cavity. In order to determine how strain influences the FSR, we take the derivative of this equation to find the relation

$$\frac{dFSR}{d\varepsilon} = -\frac{c}{\left(nl + NL\right)^2}\left(n\frac{dl}{d\varepsilon} + l\frac{dn}{d\varepsilon}\right). \tag{4.3}$$

Its differential form can be written as

$$\Delta FSR = -\frac{c}{\left(nl + NL\right)^2}\left(n\Delta l + l\Delta n\right), \tag{4.4}$$

and $(l - l_o)=\varepsilon \cdot l_o$ is substituted for Δl and $(n - n_o)=\varepsilon \cdot Q$ is substituted for Δn to gain

$$\Delta FSR = -\frac{c}{\left(nl + NL\right)^2}\left(nl_o + lQ\right)\varepsilon. \tag{4.5}$$

Equation (4.5) indicates the change in cavity FSR (ΔFSR) from the zero-strain value for an induced strain ε on fiber segment *l*. The subscript '*o*' represents the zero-strain value. The beat frequencies ($\Delta \nu_{ESA}$), measured by the ESA in Figure 4.1, correspond to ΔFSR as the first harmonic and higher-order harmonics due to the presence of a multiplicity of cavity modes. Since a larger frequency shift is measured than just one ΔFSR, a higher-order harmonic is utilized to improve the resolution of the measurement, thereby greatly reducing the measurement uncertainty. As matter a fact, the measured frequency becomes a multiple of ΔFSR and is related to the harmonic number *M* in the following way:

$$\Delta \nu_{ESA}^{M} = M\Delta FSR = -M\frac{c}{\left(nl + NL\right)^2}\left(nl_o + lQ\right)\varepsilon. \tag{4.6}$$

The SOC term Q is the only unknown in Equation (4.6), and its value can be determined from a set of measurements of $\Delta\nu^{M}_{ESA}$ vs. ε. Arbitrarily selecting M=86 is presented in the measurements. The lager M value can provides a higher accuracy to determine a Q value.

4.3.2 Determination of strain-optic coefficient

The Sumitomo Z Fiber (pure silica core) and P_2O_5-doped fiber were tested for their SOC utilizing the ring laser apparatus in Figure 4.1. The Z Fiber was tested in order to validate the SOC values assumed above for pure silica [27], while measurements on the P_2O_5-doped fiber were used to determine the SOC of bulk P_2O_5. Some specifications and measurement results are provided in Table 4.1. The modal indices were calculated from the refractive index profile using an additive model and an eigenvalue problem, and the strained fiber length was measured. *NL* was determined by measuring the FSR of the unstrained cavity and utilizing Equation (4.2) to solve for *NL* by subtracting $n_o l_o$.

Table 4.1: Selected specifications and measurement results.

Optical fiber	n_o (modal index)*	l_o (m)	*NL* (m)	SOC (Fiber)**
Z Fiber	1.440265	2.515	58.92	0.194
P_2O_5-doped Fiber	1.445509	2.502	58.65	0.189

* Calculated from refractive index profile

** The maximum error between the theoretical and measured (best-fit) slopes of the *ΔFSR* vs. strain curves for the Z Fiber and P_2O_5-doped fiber are 0.044% and 0.048%, respectively. The maximum best-fit error between the theoretical and measured individual data points in the *ΔFSR* vs. strain curves for the Z Fiber and P_2O_5-doped fiber are 2.25% and 1.93%, respectively.

Figure 4.5 shows the measured change in FSR (ΔFSR) as a function of the strain (%) for (a) the Z Fiber and (b) the P_2O_5-doped fiber. The 86^{th} harmonic was utilized for the measurements, and therefore this value was applied as a divisor to the data in order to determine ΔFSR via Equation (4.6). As a representative example, Figure 4.6 shows the actual measured data from the ESA for each of the Z Fiber data points provided in Figure 4.5(a). It has to be pointed out that the spectrum combines the beat frequencies measured at different times and they overlap together to show how FSR changes with strain.

The dashed line in Figure 4.5 is provided to perform a least-squares fit of Equation (4.6) to the measured data. In both cases (a) and (b), the R-squared value is greater than 0.999. Since the only unknown in Equation (4.6) is the SOC through Q, defined in Equation (4.13) [36], where the refractive index n is taken from Table 4.1, the SOC becomes the only fitting parameter. The resulting SOCs for the two fibers are provided in Table 4.1. The value (0.194) for the Z Fiber is very close to the value SOC $[=p_{12}-\sigma\cdot(p_{11}+p_{12})]=0.1936$, assumed previously for pure silica with Pockels coefficients $p_{11}=0.113$ and $p_{12}=0.252$, Poisson ratio $\sigma=0.16$ [27], and zero-strain refractive index $n_o=1.443$ [25], providing confidence in our use of that value in the simulations.

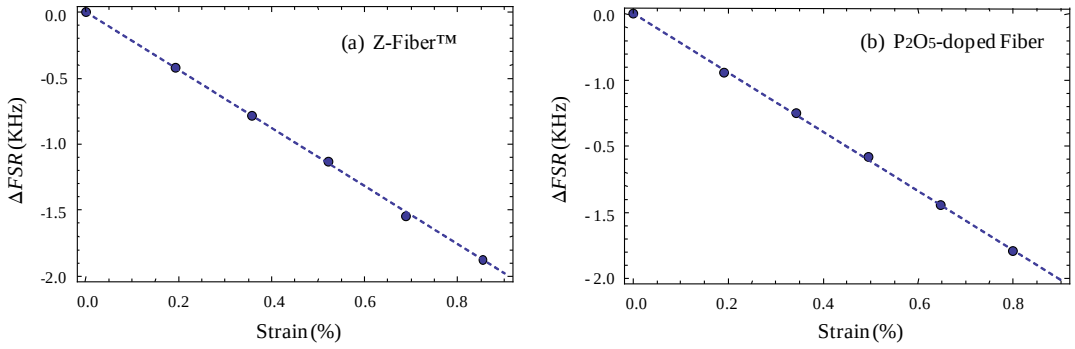

Figure 4.5: Measured (points) change in FSR as a function of strain for (a) the Z Fiber and (b) the P_2O_5-doped fiber. The dashed line is the least-squares fit of Equation (4.6) to the data.

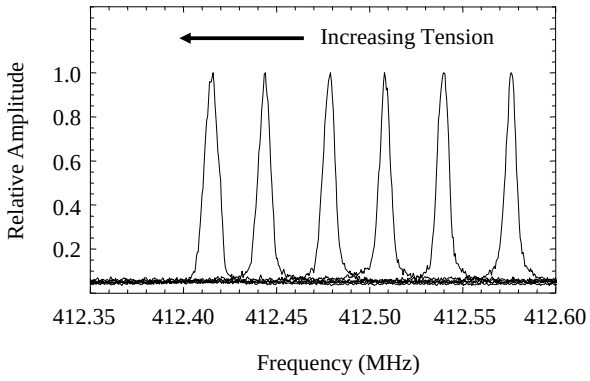

Figure 4.6: Data taken from the ESA for the Z Fiber for the data points shown in Figure 4.5 (a). The measurements were made on the 86th harmonic of the FSR (cavity mode) beat signal.

In order to calculate the SOC of bulk P_2O_5 from the fiber data, one has to utilize a step-wise approximation to the refractive index profile, and the additive model is applied to each layer to determine the index of the doped material. The approach is identical to that in [25], except that

the change in bulk refractive index values due to strain of the P_2O_5 and SiO_2 constituents now takes the form of Equation (4.6). Thus, the refractive index of each layer can be determined as a function of strain, and from this the modal index can therefore be calculated as a function of strain. Since the SOC of pure silica has already been assumed, the SOC of the bulk P_2O_5 component in the additive model is the only remaining unknown, and is adjusted until the calculated SOC (modal value) of the P_2O_5-doped fiber matches that of the measurement in Table 1. The best-fit to the measured data is an SOC of bulk P_2O_5 of +0.139 with −0.019% error [36] through the additive model [20]. A similar approach will be utilized for the SAC later.

This value is less than that of both glassy GeO_2 [62] and bulk silica [27], and will be utilized throughout the remainder of this analysis. The parameters used for the step-wise approximation can be found in Table 2 in [25]. As a convenience, Table 4.2 provides the refractive index values utilized in the calculation. The values at 0.80% strain for the six layers are shown in Table 4.2, compared with the zero-strain case, since this was the largest applied strain during the SOC measurements on the P_2O_5-doped fiber. The remaining parameters required for the additive model calculations are identical to those found in [25].

Table 4.2: Refractive index of the layers of the step-wise approximation to the RIP of the P_2O_5-doped fiber.

Layer	$[P_2O_5]$ (mol%)	V_L (ε=0) (m/s)	V_S (ε=0) (m/s)	Δn* (ε=0) (10^{-3})	V_L* (ε=0.8%) (m/s)	V_S* (ε=0.8%) (m/s)	Δn* (ε=0.8%) (10^{-3})	ρ (kg/m^3)	a (μm)
1	12.2	5331	3348	10.211	5503	3456	10.3231	2244	1.15
2	11.0	5380	3381	9.3377	5556	3492	9.4406	2240	1.70
3	8.3	5501	3458	7.2600	5687	3576	7.3401	2231	2.20
4	3.5	5751	3616	3.2466	5959	3747	3.2824	2214	2.50
5**	2.0	5843	3673	1.8567	6059	3810	1.8772	2208	8.00
6	0	5970	3749	0	6198	3892	0	2200	∞
SiO_2 Cladding	0	5970	3749	1.4430***	6198	3892	1.4407***	2200	-
P_2O_5	100	3936	2471	1.4468****	4013	2520	1.4445****	2390	-

* These V_L and V_S values correspond to SAC=9854m/s/ε and the bulk refractive index of silica is assumed to be 1.443 at 1534 nm [25].

** Due to the presence of an F-doped inner cladding, $\Delta n = -0.0005$ is used in the simulation is due to the presence of fluorine [25].

*** Absolute bulk index values at different strains

****Absolute modal index values at different strains

4.3.3 Estimate of the Pockels coefficients

Brillouin gain measurements are performed with narrow-linewidth power transmission testing to estimate the Pockels Coefficient (photoelastic constant) p_{12}. The apparatus utilized for this measurement is provided in Section 4.1.2. The Brillouin gain is calculated using the following well-known equation [1]

$$g_B(\nu_B) = \frac{2\pi n_o^{\,7} p_{12}^2}{c\lambda_o^2 \rho V_A \Delta\nu_B}\Gamma \tag{4.7}$$

where c is speed of light and the other quantities are defined in Table 4.3. g_B can be determined from measuring the back-scattered SBS power as a function of launched power in a test fiber, which has the form given by

$$P_s(z=0) = P_{s,in}^{eff} \exp\left(\frac{g_B P_p L_{eff}}{A_{eff}} - \alpha_o L\right) \tag{4.8}$$

assuming an un-depleted pump [38] and utilizing a fit-to-data. Here, $P_{s,in}^{eff}$ is an effective Stokes input power [1], P_p is the launched pump power, A_{eff} is the effective area of the optical mode, α_o is the optical attenuation coefficient (units of m^{-1}), and L is the actual fiber length. In addition, the effective length L_{eff} is calculated from

$$L_{eff} = \frac{1}{\alpha_o}\left(1 - \exp(-\alpha_o L)\right). \tag{4.9}$$

In Equation (4.7) Γ describes a normalized overlap integral between the optical and acoustic waves and is calculated for the fundamental acoustic mode (L_{01}) using

$$\Gamma = \left[\int E^*(r)E(r)u(r)rdr\right]^2 \tag{4.10}$$

where $u(r)$ is the power-normalized acoustic displacement vector and $E^*(r)E(r)$ is the normalized optical power distribution. Due to the normalized quantities, Γ takes on values between zero and one.

The results of the power transmission measurements for a fiber of length L = 54 m and the fit to experiential data points is shown in Figure 4.7.

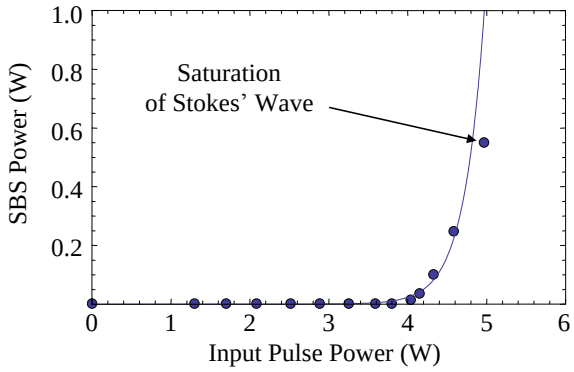

Figure 4.7: Measured and fitted SBS power vs. input pump power for a 54 m segment of the P_2O_5 fiber.

Some depletion of the Stokes signal is found at the higher powers, and thus the fit is limited to the lower-power end of the data set. In addition, the power readings contain a significantly increased instability at higher powers when significant SBS is present, which further justifies limiting the fit to the lower-power data points.

The mode field diameter (MFD) of the P_2O_5-doped silica fiber was measured to be 7.6 μm at 1550 nm by the transmitted near-field method on an EXFO NR-9200 Optical Fiber Analyzer [36]. The spatial resolution is 0.2 μm and the uncertainty on the MFD is 0.5 μm. The effective area (A_{eff}) is then calculated from this measurement of the MFD. Owing to the low-loss nature of the fiber, the effective length (L_{eff}) is calculated to be 53.2 m close to the fiber length. Through Equation (4.8) and given parameters, the effective input Stokes power ($P_{s,in}^{eff}$) is calculated to be ~ 4.4 nW [1]. The resulting fitted gain (g_B) coefficient is consequently found to be ~ 0.5 ±0.03 × 10^{-11} m/W. The assumptions made for this calculation are outlined in Table 4.3. Since the dominant acoustic mode is the fundamental mode (L_{01}), values that are characteristic of this mode are utilized [25]. Finally, Equation (4.7) is utilized to estimate p_{12} with estimated g_B and other parameters in Table 4.3. Obtained is a value of around 0.255 for p_{12} for the P_2O_5-doped fiber.

Here we describe two more assumptions used for this analysis. First, in order to remove a broadening uncertainty on the spectral width (69 MHz) of the L_{01} acoustic mode due to a length-

wise fiber with compositional variations, the BGS was measured for a long segment of fiber (54 m), which is longer than that (~3 m) in section 3.1 and the resulting L_{01} acoustic mode values were utilized in the p_{12} calculation [36]. Second, the overlap integral is determined by first fitting a series of Lorentzian functions to the spectrum. It is assumed that the total integrated Brillouin gain is unity [63], and the following expression for Γ with a total of N modes is used to fit the BGS

$$\Gamma = \frac{A_{01}\Delta\nu_B^{01}}{\sum_{m=1}^{N} A_{0m}\Delta\nu_B^{0m}} \tag{4.11}$$

where the A_{0m}'s represent the relative amplitudes of mode m.

Table 4.3: Parameters utilized to calculate p_{12}

Parameter Name	*Symbol*	*Value*
Acoustic Velocity	V_A	5376 m/s
Optical Wavelength	λ_o	1550 nm
Density*	ρ	2244 kg/m^3
Brillouin Spectral Width**	$\Delta\nu_B$	69 MHz
Overlap Integral**	Γ	0.55
Refractive Index***	n_o	1.4455
Calculated Photoelastic Constant	p_{12}	0.255±0.008

*From the central region of the core. The density of pure silica is 2200 kg/m^3.
**These values were re-measured for the longer fiber utilized in these tests.
***Taken as that of the optical mode involved in the SBS interaction (calculated).

Due to the similarity of p_{12} of silica [27] to that of the P_2O_5-doped fiber, p_{12} for silica and phosphorus pentoxide are approximately equivalent based on the additive model applied to the P_2O_5-SiO_2 binary system. Therefore, utilizing a Poisson ratio (σ) of 0.294 [33], p_{12} of 0.252, and an SOC of +0.139 for bulk P_2O_5 from Section 4.3.2, a value of 0.132 for p_{11} is obtained. Here each value is also associated with an uncertainty [36]. An extensive search on the photoelastic constants of phosphorus pentoxide, phosphate glasses, and silicophosphate (phosphosilicate) glasses has been performed. The results have not been able to reliably estimate the Pockels coefficients for P_2O_5 from the literature in order to compare with our data. Alternatively, two

pieces of evidence are consistent with our observations and findings. The first, our p_{12} - p_{11} has a positive value, consistent with the report in [64]. The second, the p_{12} - p_{11} value (0.120) of our findings is slightly less than these (0.124~0.158) of GeO_2 [62,65] and (0.134~0.149) of SiO_2 [27,65,66]. Therefore, it is suggested that our estimate of p_{11} falls within a reasonable range.

4.4 Strain-Acoustic Properties

4.4.1 Strain-acoustic frequency

In order to study the strain effect on the acoustic properties of the P_2O_5-doped silica fiber at different strains, measured was the Stokes shift of the fundamental acoustic modes (L_{01}) in the P_2O_5-doped fiber, standard GeO_2-doped SMF-28 fiber, and Z Fiber, the latter two fibers as reference fibers. The Brillouin spectra were measured up to around 1% elongation over a linear and elastic region at 1534nm. The results are shown in Figure 4.8. The fundamental mode dominates the strain sensitivity and the other higher order modes are less significant effect on the strain-acoustic properties. Thus, L_{01} is adequate to represent the strain sensitivity of these fiber samples.

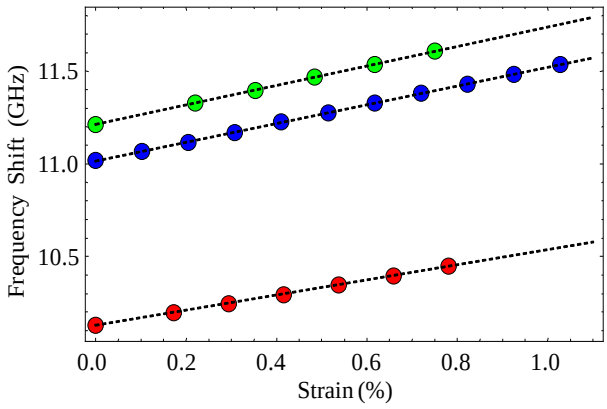

Figure 4.8: Frequency shift (fundamental mode, L_{01}) vs. strain for the P_2O_5-doped fiber (red dots), a sample of standard GeO_2-doped SMF-28 (blue dots), and pure silica fiber (Z Fiber, green dots). All R-squared values for the fits-to-data (dashed lines) are greater than 0.999. The trends are both approximately linear in the available strain range with the Stokes shift increasing and the Stokes frequency shifts are highly sensitive to the tensile strain.

The experimental results show that these fiber samples are linear and elastic systems under the tension range, and the acoustic frequency increases with increasing tensile strain. Additionally, the results imply that the Stokes frequency shift is also a function of the length increment and highly sensitive to the tensile strain. However, the slopes of these fibers are at different rates for the various fibers. It is found that the Stokes frequency shift increases at a rate of ~ +506 MHz/% for SMF-28 fiber (blue dots) and at a rate of ~ +407 MHz/% for the P_2O_5-doped fiber (red dots) at 1534nm. The result shows the strong strain-dependencies in SMF-28 fiber is roughly linear. This is consistent with the strongly dependent relationship observed in the previous report on GeO_2-doped fibers [30]. Both of these values are less than that (525 MHz/%) of pure silica fiber (Z Fiber, green dots). Stokes frequency shift is found to be much less dependent on strain in P_2O_5 than in SMF-28 as well as in pure silica fiber.

We also point out that the rate-of-change for standard GeO_2-doped SMF-28 fiber is much higher than for P_2O_5-doped silica fiber. The results indicate that the dopants each significantly, but differently, influence the strain sensitivity. The data provide a direction for the design of specialty fibers for strain sensor systems. Interestingly, the pure silica fiber data suggest that silica may have the largest strain sensitivity of all the common fiber materials. It is worth investigating other dopants and concentrations to verify this observation. In light of the feasibility and commercialization for the strain sensors, SMF-28 could be more useful for this application through monitoring the change of the acoustic frequency with strain variation which the fiber sensors experience. However, the difference of the slope is probably caused by the difference in the diameter of the core, density, index of refraction, acoustic velocity and so on. This will be further investigated by measuring the other fibers like large mode area (LMA) fibers and different doping fibers.

4.4.2 Strain-acoustic coefficient

In order to extract the strain acoustic coefficient of bulk P_2O_5, the HOAMs in the core at different strains are also considered. To the best of our knowledge, there is as yet no attempt to determine this coefficient in the literature. Following a modeling method similar to that in

Section 4.3 [25], the strain dependency of the Stokes shift for all the acoustic modes in the core is investigated.

To first order, it is assumed that only the acoustic velocity (V_A) and refractive index (n) are strain-dependent. These give rise to a strain-dependence of the calculated Stokes shift (ν_B) and modal index (n_{modal}). Thus, the strain dependence of the Brillouin frequency (ν_B) on optical wavelength (λ_o), acoustic velocity (V_A), and refractive index (n) is given by

$$\frac{d\nu_B}{d\varepsilon} = \frac{2}{\lambda_o}\left[n\frac{dV_A}{d\varepsilon} + V_A\frac{dn}{d\varepsilon} \right]. \tag{4.12}$$

As a side note, since the P_2O_5 concentration is different for each layer shown in Table 4.2, the compositional profile is approximated step-wise with six layers. Each layer will have a unique SOC and SAC. Each of these will contribute to the SOC and SAC of P_2O_5-doped silica fiber, and the various modal (optical and acoustic) quantities are calculated for each strain. Other relevant quantities are assumed to be negligibly dependent on the strain. Investigating all four observed acoustic modes simultaneously increases the confidence of the determined value.

Meanwhile, p_{11}=0.113, p_{12}=0.252, and σ=0.16 (Poisson ratio) [27] are used for the strain-dependent refractive index of bulk pure silica, and the refractive index at zero strain and room temperature is offset to n_o=1.443 in accordance with the previous work assumption [25]. The change in the refractive index as a function of induced strain can be expressed as [67]

$$Q = \frac{dn}{d\varepsilon} = -\frac{1}{2}n_o^3\left[p_{12} - \sigma\cdot(p_{11}+p_{12}) \right] \tag{4.13}$$

which is calculated from the Pockels coefficients p_{11} and p_{12}, the Poisson ratio σ, and the zero-strain refractive index n_o. Here, the strain-optic coefficient is defined to be SOC= $p_{12}-\sigma\cdot(p_{11}+p_{12})$ [36]. Despite an extensive literature search, we could not find a reported SOC for bulk P_2O_5. This can be attributed to the difficulty in working with the bulk material due to its being highly hygroscopic [60]. On the other hand, the SOC values of bulk SiO_2 and silica fiber (SOC=0.1936 if p_{11}=0.113, p_{12}=0.252, σ=0.16) can found in [27].

In section 4.3.2 the SOC of bulk P_2O_5 is determined to be +0.139 and the relative refractive index of bulk P_2O_5 at zero strain and room temperature is shown in Table 4.2; therefore, one can gain the refractive index of P_2O_5 at different strain and different concentrations for simulating the

P_2O_5-SiO_2 mixture via the additive model. In addition, it is assumed that the strain-optic effect of phosphorus dominates fluorine in the fifth layer in Table 4.2 at higher strain due to the insignificant strain-optic effect of fluorine with very low concentration in silica glass as in the present case, and the fundamental acoustic mode is most tightly confined to the center of the fiber as in the previous analysis [25].

4.4.2.1 SAC of pure silica optical fiber

After obtaining the stain dependency of the refractive index, according to Figure 4.8 results, it is reasonable to assume that the bulk acoustic velocity of both P_2O_5 and SiO_2 are linearly related to the strain (over the measured range) for modeling the acoustic velocities. For P_2O_5 the strain-dependent acoustic velocity can be written as

$$V_A^{P_2O_5}(\varepsilon) = R_P \cdot \varepsilon + 3936.00\text{m/s} \tag{4.14}$$

where R_p is strain-acoustic coefficient ($R_p \equiv SAC_p$) of bulk P_2O_5 (units of m/s/ε) and ε is fractional strain. Note that % as a unit for strain is used in Figure 4.8, but a fractional unit for strain is used in Equation (4.14) and Equation (4.16).

Similarly, Figure 4.8 shows a linear best-fit to the measured Brillouin frequency shift of the Z Fiber as a function of strain. The fit-to-data for the pure silica fiber in Figure 4.8 is given by

$$\nu_B^{SiO_2}(\varepsilon(\%)) = 524.66\,\text{MHz}/\% \cdot \varepsilon(\%) + 11.213\text{GHz} \tag{4.15}$$

where ε is percentage strain. One can extract a strain-dependent linear equation of acoustic velocity for SiO_2 from measurements of frequency vs. strain on a commercial pure silica core fiber (Sumitomo Z Fiber). More specifically speaking, utilizing the calculated strain-dependent modal index for the Z Fiber, this linear equation (Equation (4.15)) can be converted to obtain the strain-dependent linear equation of acoustic velocity for pure silica as

$$V_A^{SiO_2}(\varepsilon) = R_S \cdot \varepsilon + 5971.33\text{m/s} \tag{4.16}$$

where R_s is strain-acoustic coefficient ($R_s \equiv SAC_s$) of bulk SiO_2 (units of m/s/ε) and ε is fractional strain.

In the strain measurement, the fundamental mode of the Z Fiber dominates the Brillouin gain spectrum, and the acoustic and optical index profiles of the Z Fiber in the core are almost uniform. Furthermore, our calculations indicate that the fundamental acoustic mode velocity is very similar to the value of the core material in the Z Fiber, and thus we assume that its modal acoustic velocity can represent the acoustic velocity of bulk pure silica (core material) without introducing significant error.

Given the SOC for silica [27], from Eqns. (4.15) and (4.16) one find that R_s = +29240m/sec/ε, where the maximum best-fit error between the theoretical and the measured points in the acoustic frequency vs. strain curve of Figure 4.8 is negligible, and thus leading to a high degree of confidence in Equation (4.16).

However, the P_2O_5-doped fiber and the Z Fiber are produced by different manufacturers with different conditions. Therefore, It is not surprising that, at the zero strain and room temperature, the acoustic velocity of pure bulk silica derived from the Sumitomo fiber (5971 m/s) differs (although only slightly) from that (5970 m/s) provided in [25]. This may be due to different thermal histories [58] or draw tensions [59]. For consistency with the present analysis, the interception in Equation (4.16) of the linear equation of the acoustic velocity is offset to 5970 m/s for the strain-dependent acoustic velocity of SiO_2. The error about ~ 1.31m/s or 0.002% is negligible.

4.4.2.2 SAC of P_2O_5-doped optical fiber

By performing a best-fit to measured data to determine R_p in Equation (4.14), each acoustic mode is calculated using the same strain-dependent six-layer approximation as before with each layer possessing a unique SAC and SOC. R_p is iterated until the error across all acoustic modes is minimized. Simultaneously fitting to all four acoustic modes increases the confidence in the determined value and leads to interesting physical conclusions while R_p is the only remaining unknown here.

The result is shown in Figure 4.9 where the solid lines correspond to the modeled data and the circles to the measured data of Brillouin frequency vs. strain. Investigating Figure 6, modes 1, 2, 3, and 4 have maximum errors 0.166%, 0.184%, 0.207%, and 0.161% in the acoustic frequencies, respectively. The slight error in frequency may be attributable to uncertainty in the

dopant profile. It is worthy to point out that frequency increases with increasing mode number. The missing data points in the fourth mode results from spectral overlap with the apparatus BGC obscuring the data. It is noted that the error of mode 4 is smaller than the other three modes where the two low-strain measured points does not count due to these acoustic frequency peaks overlapping with the apparatus peaks. This case is the same as the previous work [25].

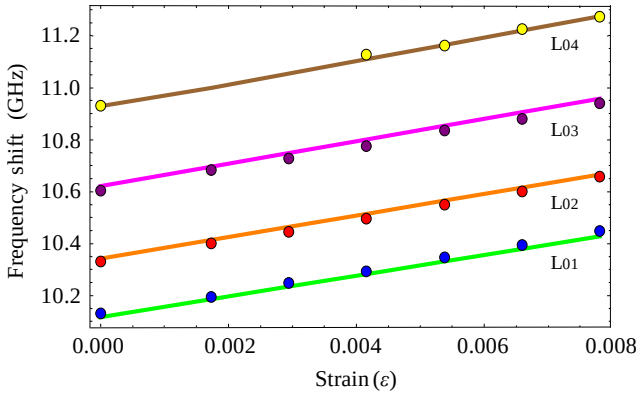

Figure 4.9: The modeled frequency shift (solid line) and the measured frequency shift (circle) vs. strain (ε). All the trends are approximately linear in the available measurement range. The modeled data of each of the modes are very close to the measured points. The fundamental mode has the lowest frequency.

Table 4.4: The comparison of measured and modeled linear equations of the strain-dependent frequency shift

Mode	Measured ν_m (Strain ε) (GHz)	Modeled ν_m (Strain ε) (GHz)	Designation
1	$40.726 \cdot \varepsilon + 10.128$ R^2=0.9994602	$39.922 \cdot \varepsilon + 10.116$ R^2=0.9999985	L_{01}
2	$41.630 \cdot \varepsilon + 10.327$ R^2=0.9988521	$41.379 \cdot \varepsilon + 10.342$ R^2=0.9999989	L_{02}
3	$42.702 \cdot \varepsilon + 10.604$ R^2=0.9989223	$43.076 \cdot \varepsilon + 10.620$ R^2=0.9999989	L_{03}
4	$43.845 \cdot \varepsilon + 10.935$ R^2=0.9971356	$44.709 \cdot \varepsilon + 10.925$ R^2=0.9996231	L_{04}

Additionally, Table 4.4 provides the strain-dependent linear equations of the measured and modeled frequency shifts for the four acoustic modes in the core. The best-fit value for R_p is obtained to be +9854 m/sec/ε. Utilizing this value, the measured and modeled slopes of the frequency versus strain curves are all within 1.974% of each other, indicating that this is a very good fit to data with 0.151% intercept-errors at the zero-strain acoustic frequency. Meanwhile, the chi-square (χ^2) test for goodness-of-fit also concludes there is extremely little difference between measured data and modeled data. Assuming that the SAC of pure silica has no uncertainty, this slope error gives rise to an uncertainty in the SAC of bulk P_2O_5 [36].

As with the temperature-dependent slope [25], there is an interesting observation. The slope of the strain curves is increasing with increasing mode number. Since the HOAMs occupy proportionally more space in the outer region of the core than the fundamental mode, where there is less P_2O_5, the slope is expected to increase with increasing mode number. This is because the acoustic velocity of silica has a much larger dependence on strain than P_2O_5 if comparing R_s= +29240m/sec/ε with R_p= +9854m/sec/ε, and, although the SAC term dominates Equation (4.12), P_2O_5 has a relatively small strain-optic coefficient, +0.139 compared to +0.194 of SiO_2.

4.5 Conclusion

In Chapter 3, we analyzed the thermal effects on P_2O_5-doped silica fiber and pure silica fiber, and we determined their thermo-acoustic coefficients. For completeness in this chapter we investigate the strain effect on P_2O_5 fiber, standard GeO_2-doped SMF-28 fiber, and pure silica (Z Fiber). Extending the work in [25] an investigation of the strain effect in P_2O_5-doped fiber is presented. From the strain coefficient measurements of a fiber with a large P_2O_5 content in the core, we have provided strain-optic coefficient for bulk P_2O_5 that is suitable for modeling purposes to determine strain-acoustic coefficient for bulk P_2O_5. It is found that the strain-optic coefficient is about +0.139, which is less than that of glassy GeO_2 [62] and bulk silica [27].

In BGS measurements of P_2O_5-doped silica fiber, the Pockels coefficients for bulk P_2O_5 are estimated. Using the measured SOC of bulk P_2O_5, the reported p_{12} of bulk SiO_2 and pure silica fiber [27], the measured p_{12} of P_2O_5-doped silica fiber, and a Poisson ratio of bulk P_2O_5 from the

literature [33], it is found that p_{11} and p_{12} of bulk P_2O_5 are 0.132 and 0.252, respectively. The data is helpful to estimate a reasonable SOC value.

In this chapter the strain coefficients for the Stokes frequency shift (fundamental mode, L_{01}) with strain are found. In strain-acoustic frequency measurements, the trends of frequency shift vs. strain for the P_2O_5-doped fiber, a sample of standard GeO_2-doped SMF-28, and pure silica fiber (Z Fiber) are approximately linear in the available strain range. The Stokes frequency shifts are highly sensitive to the tensile strain, but less so in the P_2O_5-doped fiber. The results show that the strain dependencies for the L_{01} acoustic mode are at rates of ~ +506 MHz/% for SMF-28 fiber, ~ +407 MHz/% for P_2O_5-doped fiber, and ~ +525 MHz/% for Z Fiber, respectively. Meanwhile, the P_2O_5 fiber is lower than that of SMF-28 by around 99 MHz/% as well as that of pure silica fiber by around 118 MHz/% at 1534nm. This result shows that P_2O_5 significantly influences the strain sensitivity of silica fiber. It could be a degree of freedom to design a specialty fiber with a minimum sensitivity to strain and an adequate sensitivity to temperature, for example.

By fitting a simple additive model to the data for the four observed acoustic modes, the strain-acoustic coefficient of bulk P_2O_5 is determined to be about +9854m/sec/ε, which is much lower than that (+29240m/sec/ε) of pure silica. Due to bulk coefficients extracted from the four observed acoustic modes, these bulk coefficients can be used to predict the strain-dependent Stokes shift of the higher-order acoustic modes with high accuracy. Meanwhile, this data are useful to design customized acoustic profiles of optical fiber for desirable applications.

CHAPTER 5

CONCLUSIONS

5.1 Summary

In Chapter 2, through Brillouin scattering theory, the main formula associated with optical and acoustic parameters are derived and developed. The relations of these parameters have been completely explained with simulation using good physical models. They provide large degrees of freedom to design fibers for different applications to utilize or suppress SBS. In the literature, the dopants demonstrated different optical and acoustic properties which have been summarized. The properties of bulk materials provide a reference to design a specialty fiber. However, waveguide effects could also influence the characteristics of an optical fiber via waveguide loss. As a matter of fact, it is inevitable to deal with this effect in waveguide design. Complete equations of thermo- and strain-/optic and acoustic properties reveal the relation among optical, acoustic, thermal, and strain properties. These equations enable us to investigate these parameters. There is a complete description for the additive model via a set of equations. This model can contain two, three, and an extended *N*-array of dopants in a silica-based system. Regarding materials, the model is simply applied to bulk dopants to form an optical fiber. But, the real application to the analysis in this thesis is much more complicated due to the modal effects on optical fiber. In order to obtain modal values of the optical fiber, the additive model is an eignvalue problem whose solution provides the modal values. Two special cases [14,51] for the additive model associated with some modifications are described.

In Chapter 3, in addition to acoustic attenuation at room temperature, the thermal effect on P_2O_5-doped silica fiber is studied. Based on the reported TOC of pure silica and bulk P_2O_5, the TACs of pure silica and bulk P_2O_5 are determined to be +0.56m/sec/°C and +0.12m/sec/°C. The acoustic frequency, refractive index, and acoustic frequency are formulated linear equations each

as a function of temperature. They can be used to design a specialty fiber for temperature sensing or other measurable physical quantities by minimizing the temperature sensitivity.

A similar analysis of strain effect on a P_2O_5-doped silica fiber is presented in Chapter 4. Due to the lack of the SOC of bulk P_2O_5, this value is obtained to be +0.139 via measurements and modeling of a pure silica fiber and a P_2O_5-doped silica fiber. Based on the SOC of pure silica and bulk P_2O_5, the SACs of pure silica and bulk P_2O_5 are determined to be +29240m/sec/ε and +9854m/sec/ε, respectively. The acoustic frequency, refractive index, and acoustic frequency are formulated linear equations each as a function of strain. They can be also used to design a specialty fiber for strain sensing or other measurable physical quantities by minimizing the strain sensitivity.

The complete study of thermal effect and strain effect on P_2O_5-doped silica fiber in this thesis provides designer with useful information about the optical and acoustic profiles of optical fibers to obtain customized specialty fibers for applications associated with Brillouin scattering.

5.2 Future Work

B_2O_3-doped fiber, pure silica fiber, GeO_2-doped fiber, and P_2O_5-doped fiber have been studied. While some of the study assumes bulk materials, in reality the present cases are complicated by the presence of other dopants and waveguide effects (described in Chapter 2), which also influence the Brillouin spectral width and the other acoustic properties to give rise to waveguiding and antiguiding characteristics. Therefore, in order to comprehend the fiber characteristics, it is necessary to further investigate their relations among the relevant optical and acoustic parameters of the fibers.

In Chapter 2, a simplified additive model (AD model) has been introduced. This model for any doping silica fiber can be used to calculate acoustic velocity, material damping coefficient, Brillouin spectral width, and Brillouin gain coefficient and to extrapolate these physical properties to higher concentrations. These parameters, each as a function of dopant concentration, can be useful for the design of an acoustic fiber [20,68]. Using the model, an analysis of the measurement of a Brillouin gain spectrum of a heavily germanium-doped optical fiber was

presented [19]. In addition, a mixed Sellmeier model for the bulk index of SiO_2 and GeO_2 has been developed and used in the refractive index calculation for any GeO_2-doped fiber [69].

However, the temperature-dependent Sellmeier model for bulk index has not been developed yet due to the lack of temperature-dependent coefficients of GeO_2 [16], while temperature-dependent coefficients of SiO_2 have been reported [55,70]. A goal of future work is to extend these models to gain temperature-dependent acoustic parameters.

In the future, experimental data and analysis results will enable us to calculate the related acoustic parameters as functions of temperature and investigate the anharmonic model [23] and structural relaxation model [71] for temperature-dependent acoustic properties over a wide range of temperatures to build a temperature-dependent model. Meanwhile, we will extend these analyses with a generalized model for several mixed materials. The final goal is to build a completely generalized temperature-dependent model for arbitrary doping fibers. Currently, these analyses suggest that the temperature-dependent Brillouin spectral width of the multiple-dopant fiber could be a composite function of that of the single-dopant bulk materials [14,49,72]. Consequently, based on the current and future research, we can build a generalized model associated with the three dimensions relations – any acoustic property, dopant, and temperature. This may prove to be useful in the design of optical fibers with tailored Brillouin properties for a number of different applications. For example, we can design novel low SBS fibers by decreasing the Brillouin gain coefficient and increasing the threshold power of high power laser systems for optical remote sensing. Alternatively, we can design specialty fibers with temperature-free or strain-free sensitivity for fiber-optic communication systems or sensing systems with special applications.

REFERENCES

[1] R.G. Smith, "Optical Power Handling Capacity of Low Loss Optical Fibers as Determined by Stimulated Raman and Brillouin Scattering," Appl. Opt. **11** (11), 2489-2494 (1972).

[2] D. Culverhouse, F. Farahi, C.N. Pannell and D.A. Jackson, "Stimulated Brillouin scattering: a means to realise tunable microwave generator or distributed temperature sensor," Electron. Lett. **25** (14), 915-916 (1989).

[3] T. Kurashima, T. Horiguchi, and M. Tateda, "Distributed-temperature sensing using stimulated Brillouin scattering in optical silica fibers," Opt. Lett. **15** (18), 1038-1040 (1990).

[4] P.D. Dragic, "Novel dual-Brillouin-frequency optical fiber for distributed temperature sensing," in *Nonlinear Frequency Generation and Conversion: Materials, Devices, and Applications VIII*, edited by Peter E. Powers, Proc. SPIE **7197**, 719710-1-10 (2009).

[5] A. Hadjifotiou and G.A. Hill, "Suppression of stimulated Brillouin backscattering by PSK modulation for high-power optical transmission," in *Optoelectronics*, IEE Proc. J. **133** (4), 256-258 (1986).

[6] C.G. Carlson, P.D. Dragic, B.W. Graf, R.K. Price, J.J. Coleman and G.R. Swenson, "High power Yb-doped fiber laser-based LIDAR for space weather," in *Fiber Lasers V: Technology, Systems, and Applications*, edited by Jes Broeng, Clifford Headley, Proc. SPIE **6873**, 68730K-1-10 (2008).

[7] P.D. Dragic, C.-H. Liu, G.C. Papen, and A. Galvanauskas, "Optical Fiber With an Acoustic Guiding Layer for Stimulated Brillouin Scattering Suppression," in *Conference on Lasers and Electro-Optics/Quantum Electronics and Laser Science and Photonic Applications Systems Technologies*, Technical Digest (CD) (Optical Society of America, 2005), paper CThZ3.

[8] K. Shiraki, M. Ohashi, M. Tateda, "Suppression of stimulated Brillouin scattering in a fibre by changing the core radius," Electron. Lett. **31** (8), 668-669 (1995).

[9] M. Ohashi and M. Tateda, "Design of a strain-free-fiber with nonuniform dopant concentration for stimulated Brillouin scattering suppression," J. Lightwave Technol. **11** (12), 1941-1945 (1993).

[10] J. Hansryd, F. Dross, M. Westlund, P.A. Andrekson, and S.N. Knudsen, "Increase of the SBS Threshold in a Short Highly Nonlinear Fiber by Applying a Temperature Distribution," J. Lightwave Technol. **19** (11), 1691-1697 (2001).

[11] N. Yoshizawa, T. Horiguchi, and T. Kurashima, "Proposal for stimulated Brillouin scattering suppression by fibre cabling," Electron. Lett. **27** (12), 1100-1101 (1991).

[12] P.D. Dragic, "Narrow linewidth fiber laser systems via Brillouin-tailored optical fiber," in *Laser Radar Technology and Applications XIV*, edited by Monte D. Turner, Gary W. Kamerman, Proc. SPIE **7323**, 73230W-1-9 (2009).

[13] M.-J. Li, X. Chen, J. Wang, S. Gray, A. Liu, J.A. Demeritt, A.B. Ruffin, A.M. Crowley, D.T. Walton, and L.A. Zenteno, "Al/Ge co-doped large mode area fiber with high SBS threshold," Opt. Express **15** (13), 8290-8299 (2007).

[14] P.-C. Law and P.D. Dragic, "Wavelength dependence of the Brillouin spectral width of boron doped germanosilicate optical fibers," Opt. Express **18** (18), 18852-18865 (2010).

[15] P.D. Dragic, P.-C. Law, and Y.-S. Liu, "Higher-order modes in acoustically antiguiding optical fiber," Microwave Opt. Technol. Lett. (submitted for publication on Jan., 2012).

[16] P.-C. Law, Y.-S. Liu, and P.D. Dragic, "Acoustic properties and temperature-dependence of GeO_2-doped silica fibers," (in preparation for being submitted to J. Non-Cryst. Solids, 2012).

[17] Y. Koyamada, S. Sato, S. Nakamura, H. Sotobayashi, and W. Chujo, "Simulating and Designing Brillouin Gain Spectrum in Single-Mode Fibers," J. Lightwave Technol. **22** (2), 631-639 (2004).

[18] C.-K. Jen, C. Neron, A. Shang, K. Abe, L. Bonnell, and J. Kushibiki, "Acoustic Characterization of Silica Glasses," J. Am. Ceram. Soc. **76** (3), 712-716 (1993).

[19] P.D. Dragic, "Estimating the effect of Ge doping on the acoustic damping coefficient via a highly Ge-doped MCVD silica fiber," J. Opt. Soc. Am. B: Opt. Phys. **26** (8), 1614-1620 (2009).

[20] P.D. Dragic, "Simplified model for effect of Ge doping on silica fibre acoustic properties," Electron. Lett. **45** (5), 256-257 (2009).

[21] P.D. Dragic and B.G. Ward, "Accurate Modeling of the Intrinsic Brillouin Linewidth via Finite-Element Analysis," IEEE Photon. Technol. Lett. **22** (22), 1698-1700 (2010).

[22] C. Krischer, "Optical Measurements of Ultrasonic Attenuation and Reflection Losses in Fused Silica," J. Acoust. Soc. Am. **48** (5B), 1086-1092 (1970).

[23] A.S. Pine, "Brillouin Scattering Study of Acoustic Attenuation in Fused Quartz," Phys. Rev. **185** (3), 1187-1193 (1969).

[24] R.E. Youngman, J. Kieffer, J.D. Bass, and L. Duffrène, "Extended structural integrity in network glasses and liquids," J. Non-Cryst. Solids **222**, 190-198 (1997).

[25] P.-C. Law, Y.-S. Liu, A. Croteau, and P.D. Dragic, "Acoustic coefficients of P_2O_5-doped silica fiber: acoustic velocity, acoustic attenuation, and thermo-acoustic coefficient," Opt. Mater. Express **1** (4), 686-699 (2011).

[26] H. Ohno, H. Naruse, M. Kihara, and A. Shimada, "Industrial Applications of the BOTDR Optical Fiber Strain Sensor," Opt. Fiber Technol. **7** (1), 45-64 (2001).

[27] A. Bertholds and R. Dändliker, "Determination of the Individual Strain-Optic Coefficients in Single-Mode Optical Fibers," J. Lightwave Technol. **6** (1), 17-20 (1988).

[28] M. Niklès, L. Thévenaz, and P.A. Robert, "Brillouin Gain Spectrum Characterization in Single-Mode Optical Fibers," J. Lightwave Technol. **15** (10), 1842-1851 (1997).

[29] S.M. Tripathi, A. Kumar, R.K. Varshney, Y.B.P. Kumar, E. Marin, and J.-P. Meunier, "Strain and Temperature Sensing Characteristics of Single-Mode-Multimode-Single-Mode Structures," J. Lightwave Technol. **27** (13), 2348-2356 (2009).

[30] T. Horiguchi and T. Kurashima, and M. Tateda, "Tensile Strain Dependence of Brillouin Frequency Shift in Silica Optical Fibers," IEEE Photonics Technol. Lett. **1** (5), 107-108 (1989).

[31] A.D. Kersey, E.J. Friebele, and R.S. Weis, "Erbium-doped fiber ring laser strain sensor," in *Fiber optic smart structures and skins V*; Proceedings of the Meeting, Boston, 1992, edited by Richard O. Claus, Robert S. Rogowski, Proc. SPIE **1798**, 280-285 (1993).

[32] S. Liu, R. Gu, L. Gao, Z. Yin, L. Zhang, X. Chen, and J. Cheng, "Multilongitudinal mode fiber-ring laser sensor for strain measurement," Opt. Eng. **50** (5), 054401-1-5 (2011).

[33] A.A. Higazy, B. Bridge, A. Hussein, and M.A. Ewaida, "Elastic constant and structure of the vitreous system ZnO-P_2O_5," J. Acoust. Soc. Am., **86** (4), 1453-1458 (1989).

[34] R.W. Boyd, *Nonlinear Optics*, 3rd ed. (Academic Press, San Diego, 2008), pp. 391-428.

[35] M.-J. Li, "Managing nonlinearity in optical fiber for high-power lasers," SPIE Newsroom: Optoelectronics & Communications, 10.1117/2.1200607.0317 (2006).

[36] P.-C. Law, A. Croteau, and P.D. Dragic, "Acoustic coefficients of P_2O_5-doped silica fiber: the strain-optic and strain-acoustic coefficients," Opt. Mater. Express **2** (4), 391-404 (2012).

[37] A.B. Ruffin, M.-J. Li, X. Chen, A. Kobyakov, and F. Annunziata, "Brillouin gain analysis for fibers with different refractive indices," Opt. Lett. **30** (23), 3123-3125 (2005).

[38] G.P. Agrawal, *Nonlinear Fiber Optics*, 2nd ed. (Academic Press, San Diego, 1995), pp.370-403.

[39] P.D. Dragic, "Tailoring of the Brillouin gain profile for fiber-based sensor systems and networks," in *Fiber Optic Sensors and Applications VI*, edited by Eric Udd, Henry H. Du, Anbo Wang, Proc. SPIE **7316**, 731607-1-10 (2009).

[40] C.K. Jen, J.E.B. Oliveira, N. Goto, and K. Abe, "Role of guided acoustic wave properties in single-mode optical fibre design," Electron. Lett. **24** (23), 1419-1420 (1988).

[41] P.D. Dragic, "Brillouin spectroscopy of Nd–Ge co-doped silica fibers," J. Non-Cryst. Solids **355** (7), 403-413 (2009).

[42] P. Dragic, P.-C. Law, J. Ballato, T. Hawkins, and P. Foy, "Brillouin spectroscopy of YAG-derived optical fibers," Opt. Express **18** (10), 10055-10067 (2010).

[43] P.D. Dragic, "Proposed Model for the Effect of Ge-Doping on the Acoustic Properties of Silica Fibers," in *Optical Fiber Communication Conference*, OSA Technical Digest (CD) (Optical Society of America, 2009), paper OWU4.

[44] P.D. Dragic, "Distributed temperature sensing via Brillouin-tailored optical fiber," in *Fiber Optic Sensors and Applications VI*, edited by Eric Udd, Henry H. Du, Anbo Wang, Proc. SPIE **7316**, 731605-1-9 (2009).

[45] N.F. Borrelli and R.A. Miller, "Determination of the individual Strain-Optic Coefficients of Glass by an Ultrasonic Technique," Appl. Opt. **7** (5), 745-750 (1968).

[46] C. Chen and J. Albert, "Strain-optic coefficients of individual cladding modes of single mode fibre: theory and experiment," Electron. Lett. **42** (18), 1027-1028 (2006).

[47] J. Schroeder, "Brillouin scattering and Pockels coefficients in silicate glasses," J. Non-Cryst. Solids **40** (1-3) 549-566 (1980).

[48] G.O. Karapetyan, L.V. Maksimov, O.V. Yanush, "Physical consequences of inhomogeneous glass structure from scattered light spectroscopy data," J. Non-Cryst. Solids, **126** (1-2) 93-102 (1990).

[49] P.D. Dragic, "Brillouin Gain Reduction via B_2O_3 Doping," J. Lightwave Technol., **29** (7), 967-973 (2011).

[50] P.D. Dragic, "Brillouin scattering enhanced fibers for distributed sensing," in *2nd Workshop on Specialty Optical Fibers and Their Applications (WSOF-2)*, edited by Juan Hernández-Cordero, Ismael Torres-Gómez, Alexis Méndez, Proc. SPIE **7839**, 783915-1-4 (2010).

[51] D.J. DiGiovanni, J.B. MacChesney, and T.Y. Kometani, "Structure and properties of silica containing aluminum and phosphorus near the $AlPO_4$ join," J. Non-Cryst. Solids **113** (1), 58-64 (1989).

[52] R.W. Boyd, K. Rzążewski, and P. Narum, "Noise initiation of stimulated Brillouin scattering," Phys. Rev. A: At. Mol. Opt. Phys. **42** (9), 5514-5521 (1990).

[53] A.D. Yablon, "Multi-Wavelength Optical Fiber Refractive Index Profiling by Spatially Resolved Fourier Transform Spectroscopy," J. Lightwave Technol. **28** (4), 360-364 (2010).

[54] M.M. Bubnov, E.M. Dianov, O.N. Egorova, S.L. Semjonov, A.N. Guryanov, V.F. Khopin, and E.M. DeLiso, "Fabrication and investigation of single-mode highly phosphorus-doped fibers for Raman lasers," in *Advances in Fiber Optics*, edited by Eugeny M. Dianov, Proc. SPIE **4083**, 12-22 (2000).

[55] G. Ghosh, M. Endo, and T. Iwasaki, "Temperature-Dependent Sellmeier Coefficients and Chromatic Dispersions for Some Optical Fiber Glasses," J. Lightwave Technol. **12** (8), 1338-1342 (1994).

[56] E.T.Y. Lee and E.R.M. Taylor, "Thermo-optic coefficients of potassium alumino-metaphosphate glasses," J. Phys. Chem. Solids **65** (6), 1187-1192 (2004).

[57] A. Koike and N. Sugimoto, "Temperature dependences of optical path length in fluorine-doped silica glass and bismuthate glass," in *Optical Components and Materials III*, edited by Michel J.F. Digonnet, Shibin Jiang, Proc. SPIE **6116**, 61160Y-1-8 (2006).

[58] R. Le Parc, C. Levelut, J. Pelous, V. Martinez, and B. Champagnon, "Influence of fictive temperature and composition of silica glass on anomalous elastic behaviour," J. Phys.: Condens. Matter **18** (32), 7507-7527 (2006).

[59] W. Zou, Z. He, A.D. Yablon, and K. Hotate, "Dependence of Brillouin Frequency Shift in Optical Fibers on Draw-Induced Residual Elastic and Inelastic Strains," IEEE Photonics Technol. Lett. **19** (18), 1389-1391 (2007).

[60] V.V. Brazhkin, J. Akola, Y. Katayama, S. Kohara, M.V. Kondrin, A.G. Lyapin, S.G. Lyapin, G. Tricot, and O.F. Yagafarov, "Densified low-hygroscopic form of P_2O_5 glass," J. Mater. Chem. **21** (28), 10442-10447 (2011).

[61] C.R. Giles, E. Desurvire, and J.R. Simpson, "Transient gain and cross talk in erbium-doped fiber amplifiers," Opt. Lett. **14** (16), 880-882, (1989).

[62] G.G. Devyatykh, E.M. Dianov, N.S. Karpychev, S.M. Mazavin, V.M. Mashinskiĭ, V.B. Neustruev, A.V. Nikolaĭchik, A.M. Prokhorov, A.I. Ritus, N.I. Sokolov, and A.S. Yushin, "Material dispersion and Rayleigh scattering in glassy germanium dioxide, a substance with promising applications in low-loss optical fiber waveguides," Sov. J. Quantum Electron. **10** (7), 900-902 (1980).

[63] B. Ward and J. Spring, "Finite element analysis of Brillouin gain in SBS-suppressing optical fibers with non-uniform acoustic velocity profiles," Opt. Express **17** (18), 15685-15699 (2009).

[64] M. Guignard, L. Albrecht, and J.W. Zwanziger, "Zero-Stress Optic Glass without Lead," Chem. Mater. **19** (2), 286-290 (2007).

[65] A.V. Anan'ev, V.N. Bogdanov, B. Champagnon, M. Ferrari, G.O. Karapetyan, L.V. Maksimov, S.N. Smerdin, V.A. Solovyev, "Origin of Rayleigh scattering and anomaly of elastic properties in vitreous and molten GeO_2," J. Non-Cryst. Solids **354** (26), 3049-3058 (2008).

[66] K. Matusita, C. Ihara, T. Komatsu, and R. Yokota, "Photoelastic Effects in Silicate Glasses," J. Am. Ceram. Soc. **67** (10), 700-704 (1984).

[67] C.D. Butter and G.B. Hocker, "Fiber optics strain gauge," Appl. Opt. **17** (18), 2867-2869 (1978).

[68] P.D. Dragic, "The Acoustic Velocity of Ge-Doped Silica Fibers: A Comparison of Two Models," Int. J. Appl. Glass Sci. **1** (3), 330-337 (2010).

[69] J.W. Fleming, "Dispersion in GeO_2-SiO_2 glasses," Appl. Opt. **23** (24), 4486-4493 (1984)

[70] D.B. Leviton and B.J. Frey, "Temperature-dependent absolute refractive index measurements of synthetic fused silica," in *Optomechanical Technologies for Astronomy*, edited by Eli Atad-Ettedgui, Joseph Antebi, Dietrich Lemke, Proc. SPIE **6273**, 62732K-1-11 (2006).

[71] O.L. Anderson and H.E. Bömmel, "Ultrasonic Absorption in Fused Silica at Low Temperatures and High Frequencies," J. Am. Ceram. Soc. **38** (4), 125-131 (1955).

[72] R.E. Strakna and H.T. Savage, "Ultrasonic Relaxation Loss in SiO_2, GeO_2, B_2O_3, and As_2O_3 Glass," J. Appl. Phys. **35** (5), 1445-1450 (1964).